



1 Advanced error diagnostics of the CMAQ and Chimere modelling 2 systems within the AQMEI3 model evaluation framework

3 Efisio Solazzo¹, Christian Hogrefe², Augustin Colette³, Marta Garcia-Vivanco^{3,4}, Stefano Galmarini⁵

4 ¹ European Commission, Joint Research Centre (JRC), Directorate for Energy, Transport and Climate, Air and Climate Unit,
5 Ispra (VA), Italy

6 ² Atmospheric Model Application and Analysis Branch - Computational Exposure Division - NERL, ORD, U.S. EPA

7 ³ INERIS, Institut National de l'Environnement Industriel et des Risques, Parc Alata, 60550 Verneuil-en-Halatte, France

8 ⁴ CIEMAT, Avda Complutense 40, Madrid, Spain

9 ⁵ European Commission, Joint Research Centre (JRC), Directorate for Sustainable Resources, Food and Security Unit, Ispra
10 (VA), Italy

11

12 **Abstract.** The work here complements the overview analysis of the modelling systems participating in the third
13 phase of the Air Quality Model Evaluation International Initiative (AQMEI3) by focusing on the performance
14 for hourly surface ozone by two modelling systems, Chimere for Europe and CMAQ for North America.

15 The evaluation strategy outlined in the course of the three phases of the AQMEI activity, aimed to build up a
16 diagnostic methodology for model evaluation, is pursued here and novel diagnostic methods are proposed. In
17 addition to evaluating the 'base case' simulation in which all model components are configured in their
18 standard mode, the analysis also makes use of sensitivity simulations in which the models have been applied
19 by altering and/or zeroing lateral boundary conditions, emissions of anthropogenic precursors, and ozone dry
20 deposition.

21 To help understand of the causes of model deficiencies, the error components (bias, variance, and covariance)
22 of the base case and of the sensitivity runs are analysed in conjunction with time-scale considerations and
23 error modelling using the available error fields of temperature, wind speed, and NO_x concentration.

24 The results reveal the effectiveness and diagnostic power of the methods devised (which remains the main
25 scope of this study), allowing the detection of the time scale and the fields that the two models are most
26 sensitive to. The representation of planetary boundary layers (PBL) dynamics is pivotal to both models. In
27 particular: *i*) The fluctuations slower than ~1.5 days account for 70-85% of the total ozone quadratic error; *ii*) A
28 recursive, systematic error with daily periodicity is detected, responsible for 10-20% of the quadratic total
29 error; *iii*) Errors in representing the timing of the daily transition between stability regimes in the PBL are
30 responsible for a covariance error as large as 9 ppb (as much as the standard deviation of the network-average
31 ozone observations in summer in both Europe and North America); *iv*) The CMAQ ozone error has a
32 weak/negligible dependence on the errors in NO₂ and wind speed, while the error in NO₂ significantly impacts
33 the ozone error produced by Chimere; *v*) On a continent wide monitoring network-average, a zeroing out of
34 anthropogenic emissions produces an error increase of 45% (25%) during summer and of 56% (null) during
35 winter for Chimere (CMAQ), while a zeroing out of lateral boundary conditions results in an ozone error
36 increase of 30% during summer and of 180% during winter (CMAQ).

37 1. INTRODUCTION

38 The vast majority of the research and applications related to the evaluation of geophysical models make use of
39 aggregate statistical metrics to quantify, in some averaged sense, the properties of the residuals obtained from
40 juxtaposing observations and modelled output (typically time series of the variable of interest). This practice is
41 rooted in linear regression analysis and the assumption of normally distributed residuals and has been proven
42 to be reliable when dealing with simple, deterministic and low-order models. Led by the rapid pace of
43 improved understanding of the underlying physics, the paradigm is however changed nowadays in that models



44 have grown in complexity and nonlinear interactions and require more powerful and direct diagnostic
45 methods (Wagener and Gupta, 2005; Gupta, et al., 2008; Dennis et al., 2010; Solazzo and Galmarini, 2016).

46 Evaluation of geophysical models is typically carried out under the theoretical umbrella proposed by Murphy in
47 the early 1990s for assessing the dimensions of goodness of a forecast: consistency (*'the correspondence*
48 *between forecasters' judgments and their forecasts'*), quality (*'the correspondence between the forecasts and*
49 *the matching observations'*), and value (*'the incremental benefits realised by decision makers through the use*
50 *of the forecasts'*) (Murphy, 1993). Since 2010, the Air Quality Model Evaluation International Initiative
51 (AQMEII, Rao et al., 2011) has focused on the quality dimension – the one most relevant to science, according
52 to Weijs et al. (2010) – of air quality model hindcast products, aiming at building an evaluation strategy that is
53 informative for modellers as well as to users.

54 Our claim is that the *value* of a model's result depends strictly on the *quality* of the model that, in turn,
55 depends on sound evaluation. The scientific problem of assessing the *quality* of a modelling system for air
56 quality is tackled by Dennis et al. (2010) who distinguish four complementary approaches to support model
57 evaluation: operational, probabilistic, dynamic and diagnostic, which are also the four founding pillars of
58 AQMEII. Several studies performed under AQMEII have focused on the operational and probabilistic evaluation
59 (Solazzo et al., 2012a,b; Solazzo et al., 2013; Im et al., 2015a,b; Appel et al., 2012; Vautard et al., 2012) and
60 more recently efforts have been expanded to the diagnostic aspect (Hogrefe et al., 2014; Solazzo and
61 Galmarini, 2016; Kioutsioukis et al., 2016; Solazzo et al., 2017).

62 Operational metrics usually employed in air quality evaluation (cfr. Simon et al., 2012 for a review) have several
63 limitations as summarised by Tian et al. (2016): *interdependence* (they are related to each other and are
64 redundant in the type of information they provide), *underdetermination* (they do not describe unique error
65 features), and *incompleteness* (how many of these metrics are required to fully characterise the error?).
66 Furthermore, they do not help to determine the *quality* problem set above in terms of diagnostic power.
67 Gauging (average) model performance through model-to-observation distance leaves open several questions
68 such as *a)* How much information is contained in the error? In other words, what remains wrong with our
69 underlying hypothesis and modelling practice? *b)* Is the model providing the correct response for the correct
70 reason? *c)* What is the degree of complexity of the system models can actually match? These questions have a
71 straightforward, very practical impact on the use of models, the return they provide (the value) and their
72 credibility. Answers to these questions are also relevant to the wide-spread practice of bias correction which is
73 aimed at adjusting the model value to the observed value, rather than correcting the causes of the bias which
74 might stem from systematic, cumulative errors.

75 The main aims of this study are to move towards tools devised to enable diagnostic interpretation, following
76 the approach of Gupta et al. (2008 and 2009), Solazzo and Galmarini (2016), and Kioutsioukis et al. (2016) and
77 to advance the evaluation strategy outlined in the course of the three phases of AQMEII. In particular, the
78 work presented here is meant to complement the overview analysis of the modelling systems participating in
79 AQMEII3 (summarised by Solazzo et al., 2017) by concentrating on the performance for surface ozone
80 modelled by two modelling systems: Chimere for Europe (EU) and CMAQ for North America (NA). This study
81 attempts to:

- 82 • Identify the time scales (or frequencies) of the error of modelled ozone;
- 83 • Attribute each type of error to processes by utilizing modelling runs with modified fluxes at the
84 boundaries (anthropogenic emissions and deposition at the surface, and boundary conditions at the
85 bounding planes of the domain) and breaking down the mean square error (MSE) into bias, variance
86 and covariance. This analysis allows us to diagnose the quality of error and to determine if it is caused
87 by external conditions or due to missing or biased parameterisations or process representations;
- 88 • Investigate the periodicity of the ozone error which can be symptomatic of recursive (either casual or
89 systematic) model deficiencies;



- 90 • Determine the role of the error of precursor or meteorological fields in explaining the ozone error.
91 The significance (or the non-significance) of a correlation between the ozone error and that of one of
92 the explanatory variables can help to understand the impact (or lack of impact) of the latter on the
93 ozone error as well as the time-scale of the process(es) causing the error.

94 Among the several models participating in AQMEII3, CMAQ and Chimere have been selected as the analysis
95 proposed in this study requires additional simulations beyond those performed by all AQMEII3 groups, which
96 implied additional dedicated resources that were not available to all groups. This of course opens an important
97 issue connected with the relevance of models in decision making, the adequacy of their contribution, and
98 consequently the fact that far more resources would be required by the present complexity and state of
99 development of modelling systems to guarantee that deeper evaluation strategies are put in place. Although
100 only these two modelling systems are analyzed here, they represent two well-established systems that have
101 been systematically developed over many years, are in use by a large number of research groups around the
102 world and also have participated in the various phases of AQMEII.

103 The data used, model features and error decomposition methodology are summarised in section 2. Results of
104 the aggregate time series and error decomposition analyses are presented in section 3 and results of the
105 diagnostic error investigation through wavelet, autocorrelation, and multiple regression analysis are presented
106 in section 4. Conclusions and final remarks are drawn in Section 5.

107 2. METHODS

108 2.1 DATA AND MODELS

109 Unless otherwise specified, analyses are carried out and results are presented for the rural receptors of three
110 sub-regions over each continental area as shown in **Figure 1**. The three sub-regions have been selected based
111 on similarity analysis of the observed ozone fluctuations slower than ~1.5 days. The regions where the slow
112 fluctuations showed similar characteristics were selected through unsupervised hierarchical clustering (details
113 in Solazzo and Galmarini, 2015). Due to the similarity of the observations within these regions which implies
114 that they experience common physical and chemical characteristics, spatial averaging within these sub-regions
115 was carried out.

116 The stations used for the analysis are part of the European (European Monitoring and Evaluation Programme:
117 EMEP; <http://www.emep.int/>; European Air Quality Database AirBase;
118 <http://acm.eionet.europa.eu/databases/airbase/>) and North American (USEPA Air Quality System AQS:
119 <http://www.epa.gov/ttn/airs/airsaqs/>; Analysis Facility operated by Environment Canada:
120 <http://www.ec.gc.ca/natchem/>) monitoring networks. Full details are given in Solazzo et al. (2017) and
121 references therein.

122 Following the approach used in previous AQMEII investigations, modelled hourly concentrations in the lowest
123 model layer (~20m for both models) and corresponding observational data are paired in time and space to
124 provide a verification data sample $\{mod_r^t, obs_r^t; t=1, \dots, 8760; r=1, \dots, n_{recs}\}$ of n_{recs} (number of monitoring
125 stations) record of matched modelled and observational data, where the r^{th} -pair $mod_r^{t_0}$ and $obs_r^{t_0}$ is evaluated
126 at receptor r at a given time t_0 . Further, while the observations are reported at the hour at the end (for
127 Europe) or at the beginning (for NA) of the hourly averaging window, the model values available in this study
128 are provided instantaneously. Therefore, the modelled data were averaged between two contiguous hours
129 and assigned to the end (or beginning) of that hour for consistency with the observations. This is of particular
130 relevance when estimating the error due to timing of the diurnal cycle discussed in section 4.3, although for EU
131 there is no harmonisation of time references.

132 For the analyses conducted in this study, the spatial average of the observed and modelled ozone time series
133 has been carried out prior to any time aggregation, i.e. the spatial average is created by averaging the hourly



134 values over all rural stations in each region. The analysis is restricted to stations with a data completeness
 135 percentage above 75% and located below 1000m above sea level. Time series with more than 335 consecutive
 136 missing records (14 days) have been also discarded. Missing values have not been imputed. The number of
 137 rural receptors n_{recs} for ozone is 38, 184, and 40 for EU1, EU2, and EU3 and 73, 43, and 28 for NA1, NA2, and
 138 NA3, respectively.

139 The configuration of the CMAQ and Chimere modelling systems for AQMEII3 is extensively discussed in
 140 Solazzo, et al. (2017) with respect to resolution, parameterisations, and inputs of emissions, meteorology, land
 141 use, and boundary conditions. For completeness a short summary is provided hereafter.

142 The CMAQ model (Byun and Shere, 2006) is configured with a horizontal grid spacing of 12 km and 35 vertical
 143 layers (up to 50 hPa) and uses the widely applied CB05-TUCL chemical mechanism (Carbon Bond mechanism,
 144 Whitten et al., 2010) for the representation of gas phase chemistry. Emissions from natural sources are
 145 calculated inline by the Biogenic Emissions Inventory System (BIES) model. The meteorology is calculated by
 146 the Weather Research and Forecast (WRF) model (Skamarock et al., 2008) with nudging of temperature, wind
 147 and humidity above the planetary boundary layer (PBL).

148 Chimere (Menut et al., 2013) is configured with a grid of 0.25 degree (~25 km x 18 km over France), 9 vertical
 149 layers (up to 500 hPa) and uses the Melchior2 chemical mechanism (Lattuati, 1997) for the representation of
 150 gas phase chemistry. Natural emissions are calculated using the MEGAN model (Guenther 2012). The hourly
 151 meteorological fields are retrieved from the Integrated Forecast System (IFS) operated by the European Centre
 152 for Medium-Range Weather Forecast (ECMWF).

153 Both models are widely used worldwide in a range of applications such as scenario analysis, forecasting,
 154 ensemble modelling, and model inter-comparison studies.

155 2.2 SENSITIVITY RUNS WITH CMAQ AND CHIMERE

156 The Chimere and CMAQ models have been used to perform a series of sensitivity simulations aimed at a better
 157 understanding of the causes of differences between the base model simulations and observed data. In
 158 particular, the following set of sensitivity runs was performed:

- 159 • one annual run with zeroed anthropogenic emissions to provide an indication of the amount of
 160 regional ozone due to boundary conditions and biogenic emissions (referred to as 'zero Emi');
- 161 • one annual run with a constant value of ozone (zero for NA and 35 ppb for EU) at the lateral
 162 boundaries of the model domain to provide an indication of amount of ozone formed due to
 163 anthropogenic and biogenic emissions within the domain (in addition to the constant value for EU)
 164 (referred to as 'zero BC' and 'const BC'). All species other than ozone had boundary condition values
 165 of zero for both NA and EU in these sensitivity simulations;
- 166 • one annual run where the anthropogenic emissions are reduced by 20%. In addition, the boundary
 167 conditions for this run were prepared from a C-IFS simulation (detail in Galmarini et al., 2017 and
 168 references therein) in which global anthropogenic emissions were also reduced by 20% (referred to as
 169 a '20% red');
- 170 • one run with ozone dry deposition velocity set to zero, available for the months of January and July
 171 (referred to as 'zero Dep').

172 2.3 ERROR DIAGNOSTIC METRIC

173 To aid diagnostic interpretation, the total quadratic error MSE ($MSE = E[mod-obs]^2$) is decomposed according
 174 to

$$MSE = (\overline{mod} - \overline{obs})^2 + (\sigma_m - \sigma_o)^2 + 2\sigma_m\sigma_o(1 - r) = bias^2 + var + covar \quad \text{Eq 1}$$



175 Where σ_m and σ_o are the modelled and observed standard deviation, *var* and *covar* are the variance and
176 covariance operators, *r* is the linear correlation coefficient, and *bias* is the time averaged offset between the
177 mean modelled and observed ozone concentration. The MSE is a quadratic, parametric metric widely applied
178 in many contexts and occurs because the model does not account for information that could produce a more
179 accurate estimate. Put in an information theory context, the MSE provides a measure of the information about
180 the observation that is missing from a Gaussian model centred at a deterministic prediction (Nearing et al.,
181 2015). Ideally, the deviation of a perfect model from the observation should be zero or simply white noise
182 (uncorrelated, zero mean, constant variance). Various flavours of MSE decomposition have been exploited in
183 several geophysical contexts (Enthekebi, et al., 2010; Murphy, 1988; Wilks, 2011; Wilmott, 1981; Gupta, et al.,
184 2009), all stemming from the consideration that the bias, the variance, and the covariance characterise
185 different (although not complementary and not exhaustive) properties of the error – accuracy, precision, and
186 correspondence, respectively.

187 The first two moments (mean and variance) relate to the systematic error (unconditional bias) and variability
188 (variance), respectively. All other differences between the statistical properties of modelled and observed
189 chemical species (e.g. the timing of the peaks and autocorrelation features) are quantified by the correlation
190 coefficient, i.e. in the covariance term (Gupta et al., 2009).

191 The relative contribution of each of the MSE components to the overall MSE is summarised by the Theil's
192 coefficients (Theil, 1961):

$$\begin{aligned} F_b &= \text{bias}^2/\text{MSE} \\ F_v &= \text{var}/\text{MSE} \\ F_c &= \text{covar}/\text{MSE} \end{aligned} \quad \text{Eq 2}$$

193 The overall MSE suffers from the limitations of the aggregate metrics discussed in the introductory section,
194 lacking independence and explanatory power (Tian et al., 2016). When decomposed (e.g according to Eq 1),
195 however, the underdetermination issue is reduced and the MSE coefficients (Eq 2) do offer diagnostic aid in
196 interpreting the modelling error (Gupta, et al., 2009).

197 3. SENSITIVITY ANALYSIS TO EMISSIONS AND BOUNDARY CONDITIONS PERTURBATIONS

198 3.1. AGGREGATED TIME SERIES OF OZONE

199 **Figure 2** and **Figure 3** show monthly and diurnal curves for the base and sensitivity simulations over the three
200 sub-regions in each continent. Results show that the monthly averaged curves of the zeroed emission runs
201 peak in April in NA and in July in EU (May to July in EU1 are approximately the same), indicating the periods
202 when the impact of background concentration (boundary conditions) and biogenic emissions on regional
203 ozone is largest: springtime in NA and summer in EU. The monthly curves of 'zero BC' and 'zero Emi' for NA are
204 anti-correlated between the months of April to July-August ('zero Emi' curve decreasing and 'zero BC' curve
205 raising) and during autumn ('zero Emi' curve rising and 'zero BC' curve decreasing), framing the interplay
206 among these two factors in terms of total ozone loading: boundary conditions dominating in autumn-winter
207 and biogenic plus anthropogenic emissions are more important during spring-summer.

208 The daily averaged profiles of mean ozone for NA show that the observed peak (occurring between 16-18 LT in
209 NA1 and NA2 and ~1 hour earlier in NA3) is preceded by the peak in the base run by ~1hour in NA2 and by ~2-
210 3 hours in NA1, while the timing of the observed minimum (occurring at 8-9 am LT) is captured by the base run
211 in NA2 and NA3 while it is preceded by the base run by ~1hour in NA1. The modelled morning transition to
212 convective conditions is in phase with the observations except for NA1 where the modelled transition occurs
213 one hour earlier than the observed one. The modelled afternoon transition in NA1 precedes the observed
214 transition by 3-4 hours, possibly due to errors in the partitioning between sensible and latent surface heat flux
215 that causes a faster-than-observed collapse of the PBL. As discussed in Appel et al. (2016), updates to the



216 stomatal conductance function and the heat capacity for vegetation in WRF and the ACM2 vertical mixing
217 scheme in both WRF and CMAQ (relative to the version of WRF and CMAQ used in the current study) lead to a
218 change in the modelled diurnal cycle of ozone as well as other pollutants and meteorological variables. In
219 particular, the updates lead to a delay in the evening collapse of the modelled PBL (Appel et al., 2016). The
220 shape of the 'zero BC' curve is similar in amplitude to that of the base run, suggesting that the effect of the
221 regional/background ozone represented through boundary conditions in a limited area model is mainly to shift
222 the mean concentration upwards while it has no major effect on the frequency modulation. By contrast, the
223 absence of anthropogenic emissions has a major effect of the amplitude of the signal as well as its magnitude
224 ('zero Emi' curve). As discussed in the next section, these considerations translate into the bias and/or variance
225 type of error due to the boundary conditions and emissions.

226 As for EU (**Figure 3**), the observed daily profiles in EU1 and EU2 are closely matched by the Chimere model
227 between 11 LT and 23 LT (underestimated outside these hours), while in EU3 the daily peak (observed at 19-20
228 LT) is consistently occurring earlier in the model and its magnitude is overestimated. The morning transition
229 occurs earlier in the model than the observations and follows a significant model under-prediction of
230 nighttime and early morning ozone, due to difficulties in reproducing stable or near-stable conditions
231 (Bessegnet et al., 2016). In EU3, the model displays the poorest performance, with significant underestimation
232 between midnight and 9 LT (5-7 ppb) and over-estimation in daylight conditions (7-9 ppb).

233 As opposed to the CMAQ case for NA, the shape of the 'zero Emi' curve of Chimere closely follows the shape
234 that of the base case (even when considering only the stations classified as 'urban', Figure S2), suggesting a
235 bias type of error.

236 Due to the long time average (one year), the daily profiles displayed in **Figure 2** and **Figure 3** do not provide
237 information about the exact timing of the minima and maxima for each season throughout the year. Figure S3
238 and Figure S4 report the seasonal average diurnal profiles for the model predictions and the observations
239 (network average over all stations) and show that the timing of the ozone diurnal cycle varies seasonally.

240 3.2. ERROR DECOMPOSITION

241 The plots in **Figure 4** (NA) and **Figure 5** (EU) show the MSE decomposition according to Eq. 1 for the summer
242 months of June, July, and August for the base case simulation as well as the sensitivity simulations,
243 distinguishing between daylight (from 5am to 9pm LT) and night-time hours (the remaining hours, from
244 10pm to 4am LT). These plots are meant to aid the understanding of the relative impacts of potential errors in
245 lateral boundary conditions, anthropogenic emissions, and the representation of ozone dry deposition on the
246 total model error by comparing the magnitude and type of model error from these simulations against the
247 model error for the base case.

248 The plots in **Figure 6** and **Figure 7** are complementary to Figures 4-5 and show the error decomposition for
249 both the summer and winter season in more detail, including the error coefficients F_b , F_v , F_c of Eq 2 (left
250 vertical axis), the total MSE (right vertical axis), the sign of the bias and variance error (+/- for model over and
251 under prediction), and the values of the correlation coefficient. Furthermore, the maps in **Figure 8** and **Figure 9**
252 show the RMSE at the receptors for the 'base' case as well as $\Delta RMSE$, i.e. the percentage change of RMSE of
253 the sensitivity runs with respect to the 'base' case simulation:

254 $\Delta RMSE = 100 * (RMSE_s - RMSE_{base}) / RMSE_{base}$, where the subscript s indicates the zeroed emission or the zeroed
255 (constant) boundary condition simulations ($\Delta RMSE$ is measured as percentage).

256 The CMAQ results for NA are presented in **Figure 4**, **Figure 6**, and **Figure 8** and can be summarised as follows:



- 257
- 258
- 259
- 260
- 261
- 262
- 263
- 264
- 265
- 266
- 267
- 268
- 269
- 270
- 271
- 272
- 273
- 274
- 275
- 276
- 277
- 278
- 279
- 280
- 281
- 282
- 283
- 284
- 285
- 286
- 287
- 288
- 289
- 290
- 291
- 292
- 293
- 294
- 295
- 296
- 297
- 298
- 299
- 300
- 301
- 302
- 303
- 304
- 305
- The MSE of the base case (MSE_{base}) during summer daylight is mainly due to bias (~35% in NA1 and ~75% in NA2 and NA3) and the remaining portion is due to covariance error. The fact that there is no variance error shows that the model is able to replicate the observed 3-month averaged variability.
 - The effect of zeroing the emissions of anthropogenic pollutants on the summer MSE is a rise by a factor ~2 to 4 (daylight) and by a factor ~6 to 7 during night-time in NA1 and NA2 with respect to MSE_{base} , while during night-time in NA3 the MSE stays approximately the same, indicating that the emissions have little role in determining the total error in this sub-region during night during summer. Furthermore:
 - All the error components deteriorate in the simulations with zero anthropogenic emissions except for the bias in NA3. This is particularly true for the variance, signifying the fundamental role of emissions in shaping the diurnal variation of ozone. Indeed, this suggests that the absence of a variance error in the base case (see above) is due to the correct intensity of the prescribed emissions;
 - The covariance share of the error also increases (although only slightly in NA2) for the zero emissions case, indicating that the emissions play a role in determining the timing of the modelled diurnal ozone signal, this increase is more pronounced during night-time.
 - The zeroing of the input of ozone from the lateral boundaries has either no effect or only a very limited effect on the variance and covariance shares of the error, while it has a profound impact on the bias portion. This impact is approximately equal during daylight and night-time, as expected from the discussion of the daily cycle shown in **Figure 2**.
 - The removal of ozone dry deposition from the model simulations (results based on July only) has the most profound impact, increasing by one order of magnitude the MSE of the base case which is approximately double the combined effect of the emissions and boundary conditions perturbation. This sensitivity gives a gross indication of the relative strength of this process vs external conditions during summer, while the 'zero BC' case has a larger effect than the 'zero deposition' case in January (not shown). Similar to the 'zero BC' case, the exclusion of ozone dry deposition from the model simulations acts as an additive term to the diurnal curve in NA1, leaving almost unaltered the shape and timing of the signal, while it impacts the variance and covariance error in the other two sub-regions.
 - The instances where the '20% red' bias error is lower than the error of the base case occur when the mean ozone concentrations were overestimated in the base case (e.g. daylight for all sub-regions and NA2 and NA3 over night-time summer) as illustrated in **Figure 6a,b**.
 - The maps show that there are stations where the error is reduced with zero anthropogenic emissions (e.g. a reduction of 20-30% in the south coast of the US and in the far North-east during summer, **Figure 8d**). This suggests the presence of other compensating model errors in both the base and sensitivity simulations that lead to better agreement with observations when prescribing an unrealistic emission scenario. The sources of these compensating errors need to be investigated in future work.
 - The 'zero BC' run has profound negative effects over the whole continental area of NA during winter (**Figure 8e**), while the effects are smaller during summer (**Figure 8f**) especially over the southern coast due to the relatively higher importance of photochemical formation of ozone during summer.
 - The error characteristics of the daily maximum 8-hour rolling mean (DM8h, **Figure 6e**) resemble those of the daylight base case (but reduced in magnitude during winter), with almost null variance error and the same sign of the bias as the base case. The error of the DM8h for the sensitivity runs is reported in Figure S5.
 - On a network-wide average, removing anthropogenic emissions causes a RMSE increase of 25% during summer and of 0% (10% at 75th percentile) during winter while a zeroing out of input from the lateral boundaries causes a RMSE increase of 30% during summer and of 180% during winter (median values, **Figure 8**).



306 The allocation of the error of the Chimere model for EU varies greatly by sub-region (**Figure 5**, **Figure 7**, and
307 **Figure 9**):

- 308 • The summer daylight $\text{RMSE}_{\text{base}}$ ranges between $\sim 20 \text{ ppb}^2$ (EU1, $\sim 60\%$ covariance and $\sim 20\%$ bias) and
309 $\sim 85 \text{ ppb}^2$ (EU3, 95% covariance). In EU3, the night-time bias of $\sim 75\%$ outweighs the covariance as
310 seen in **Figure 7a**.
- 311 • Removing the anthropogenic emissions had almost no effect on the covariance share of the MSE (if
312 not a slight reduction with respect to the base case in EU2 and EU3, and also during night-time),
313 indicating that the error in the timing of the signal is not influenced by the emissions but rather by
314 other processes. Moreover, the variance portion is left almost unchanged (1 ppb increase in EU1 and
315 EU2), in contrast with the CMAQ results for NA. This would indicate that the variability of ozone
316 concentration is hardly influenced by anthropogenic emissions in Chimere. The bias is the error
317 component most sensitive to emissions reductions, especially in EU2 and less so in EU3. This is in line
318 with the discussion of the daily profiles of **Figure 2b** (which showed similar shapes of for the 'zero
319 Emi' and of the 'Base' profiles) and contrasts with the NA case where the 'zero Emi' daily profiles are
320 flatter than the base case.
- 321 • The effect of imposing a constant ozone boundary condition value of 35 ppb (and of zero for all other
322 species) on the model error is similar to that of removing the anthropogenic emissions as far as the
323 total MSE and the bias of EU2 are concerned. It outweighs the latter for the total MSE, bias and
324 variance in EU3 and covariance and night-time bias component in EU1. We can infer that the
325 boundary conditions have a significant role in determining the timing of the ozone signal in EU1 (close
326 to the western boundary of the domain) as the correlation coefficient degrades from 0.89 (base case)
327 to 0.66 ('const BC') (**Figure 5** and **Figure 7a** and c). The bias staying the same in EU1 daylight summer
328 depends on the magnitude of the constant value (35 ppb were chosen here) that is in close
329 agreement with that of the base case while the small variance error ($\sim 2 \text{ ppb}$) vanishing with respect to
330 the base case might be explainable with numerical compensation.
- 331 • During summer in EU2 and EU3 changing the ozone boundary condition only influences the bias with
332 marginal impacts on variance and covariance, while in winter (**Figure 7c**) there is also a significant
333 reduction of the correlation coefficient, meaning that the boundary conditions modulate the timing of
334 the signal.
- 335 • EU3 deserves special consideration as the $\text{RMSE}_{\text{zeroEmi}}$ is approximately the same as the $\text{RMSE}_{\text{base}}$,
336 which mostly consists of covariance error during daylight and bias error during night-time. Due to the
337 local topography, EU3 is typically characterised by stagnant conditions that are difficult to model. For
338 example, 50% of the observed wind speed is below 1.65 ms^{-1} , while Chimere predicts 1.95 ms^{-1} . The
339 largest impact on the total MSE is seen in the 'const BC' run and arises in the bias portion, pointing to
340 the importance of properly characterising background (regional) concentrations.
- 341 • With respect to the base case, the DM8h (**Figure 7e**) shows a drastically reduced covariance error (the
342 timing error is now shifted towards seasonal time scales) at the expense of an increase in variance
343 error. The variability of the DM8h is governed by synoptic processes which are likely responsible for
344 the variability error of the DM8h. The error of the DM8h for the sensitivity runs is reported in Figure
345 S6.
- 346 • On a network-wide average, removing anthropogenic emission causes an RMSE increase of 45%
347 during summer and of 56% during winter (median values, **Figure 9c,d**).
- 348 • The effect of setting the dry deposition velocity of ozone to zero (July only, **Figure 5**), increases not
349 only the bias error but also causes large increases of the variance and covariance shares of the error.
350 Thus in Chimere the deposition acts not only as a shifting term on the modelled concentration but it
351 also influences the variability and timing of ozone more profoundly than for the CMAQ case examined
352 earlier.



353 4. TIME-SCALE ERROR ANALYSIS AND DIAGNOSTIC

354 The focus of this section is ΔO_3 , the time series of the deviation between the base case and observations. The
355 nature of ΔO_3 is examined for time-frequency patterns using wavelet analysis and for error persistence using
356 autocorrelation functions (ACF). The causes of ΔO_3 are also tentatively investigated as dependencies on other
357 fields using multiple regression analysis combined with bootstrapping to sample the relative importance of the
358 regression variables.

359 4.1. SPECTRAL CONSIDERATIONS

360 The coefficients of the ACF (Appendix 1) can be interpreted as the Fourier transform of the power spectral
361 density. Frequency analysis of a signal is often performed by constructing the periodogram (or spectrogram,
362 see e.g. Chatfield, 2004). This approach has proven useful when dealing with harmonic processes
363 superimposed on a baseline signal (Mudelsee, 2014) but, at the same time, periodograms often contain high
364 noise. Therefore, examining a signal at specific frequencies can be instructive, for instance by resorting to
365 wavelet transform which has the further advantage of enabling a 3-dimensional time-frequency-power
366 visualisation. Compared to a power spectrum showing the strength of variations of the signal as function of
367 frequencies, wavelet transformation also allows the allocation of information in the physical time dimension
368 other than phase space. Here, wavelet analysis of the periodogram of seasonal ΔO_3 is performed using the
369 Morlet wavelet transform (Torrence and Compo, 1997).

370 From inspecting **Figure 10** (NA) it emerges that the highest values of spectral energies for ΔO_3 for the three
371 sub-regions (corresponding to the 99th percentile of the spectrum) are observed for periods spanning the
372 whole year, associated with the slow variability of the non-zero bias throughout the investigated period. Such
373 a process is more evident in NA1 and NA2 and its magnitude is one order of magnitude (or more) of the 90th
374 percentile value.

375 NA3 and to a lesser extent NA2 show a high spectral power of the error for periodicities of 1-2 months and
376 lasting from January to May with a weaker wake extending up to the end of the year, potentially pointing to
377 errors in the characterisation of larger-scale background concentrations associated with boundary conditions.
378 NA3 also exhibits a high spectral power for errors associated with a periodicity of ~20 days during January-
379 February and June-July and ~ 15 days during October and December. This may point to errors in representing
380 the effects of changing weather regimes on simulated ozone concentrations.

381 Except for the long-term variations of the model error with periodicities greater than 2 months discussed
382 above, NA1 is the only sub-region that shows only weak power associated with model errors of shorter
383 periodicities from June to December. This suggests that fluctuations caused by variations in large scale
384 background and changing weather patterns are better captured in this region compared to the other two sub-
385 regions.

386 The energy associated with the daily error is again higher and more pronounced in NA3 than in the other sub-
387 regions where it is most pronounced during summer (NA1) or between March to October (NA2). While during
388 winter and autumn the daily error is likely driven by difficulties in reproducing stable PBL dynamics, during
389 spring and summer it is also influenced by the chemical production and destruction of ozone, a process
390 entailing NO_x chemistry, radiation, biogenic emission estimates and chemical transformation, and thus difficult
391 to disentangle from boundary layer dynamics.

392 For the EU (**Figure 11**) a notable feature is the very high daily error energy in EU3 that is present throughout
393 the year and most pronounced in summer. Such high energy suggests persistent problems in representing
394 processes having a periodicity of one day. Further, EU3 shows an area of high energy associated with a period
395 of one to two months and extending from February, peaking in April and May, and ending in September
396 (mostly model underestimation, **Figure 11c**), while the error of the winter months in EU3 receives high energy



397 from slower processes, acting on time scales of ~6 months and beyond. Considering that the EU3 region is
398 surrounded by high mountains, tropopause folding (e.g. Bonasoni et al., 2000; Makar et al., 2010) together
399 with the lack of modelling mechanisms for the tropopause/stratosphere exchange, could offer an explanation
400 of the high energy of the error at long time scales (also considering that the higher level modelled by Chimere
401 is well below the tropopause and that vertical fluxes are those prescribed by the C-IFS model). Errors in
402 estimates of biogenic emissions also remains a plausible cause of ozone error during spring and summer
403 months.

404 The similarity of the wavelet spectra for NA3 (Figure 10c) and EU1 (Figure 11a) (both regions are located on
405 the Western edge of their domain) at the beginning of the year for periods of 1 to 2 months might be
406 indicative of the periodicity of the bias induced by the boundary conditions. Compared to CMAQ, the error of
407 the Chimere model is more concentrated during spring and early summer, with a periodicity of 10-20 days.

408 Having identified some relevant time-scales for the ΔO_3 error, in the next sections methods are proposed for
409 its detection and quantification.

410 4.2. TEMPORAL CHARACTERISTICS OF THE ERROR OF OZONE

411 In a recent study, Otero et al. (2016) analyzed which synoptic and local variables best characterise the
412 influence of large scale circulation on daily maximum ozone over Europe. The authors found that the 24-hour
413 lag autocorrelation explains the majority of the variance during spring over the entire EU continent while
414 during summer the maximum temperature is the principal explanatory variable over continental EU. Other
415 influential variables were found to be the relative humidity, the solar radiation and the geopotential height.
416 Camalier et al. (2007) and Lemaire et al. (2016) found that the near-surface temperature and the incoming
417 short-wave radiation were the two most influential drivers of ozone uncertainties.

418 The ACF and PACF (partial autocorrelation function) of ΔO_3 (see Appendix 1 for a definition of both functions)
419 reveals a strong periodicity for periods that are multiples of 24 hours (Figure 15a And Figure 16a) (note that
420 the first derivative of ΔO_3 is used in this analysis to achieve stationarity). The structure of the error is such that
421 it repeats itself with daily regularity, indicating either a systematic error in the model physics or a missing
422 process at the daily scale, possibly related to radiation and/or PBL-related variables. While the presence of a
423 daily periodic forcing due to the deterministic nature of day/night differences superimposed on the baseline
424 ozone is expected, the periodicity maintained in the error structure is not and deserves further analysis.

425 The PACF plots confirm that the error is not simply due to propagation and memory from previous hours, but
426 arises at 24h intervals and hence stems from daily processes. On average, for NA $corr(\Delta O_3(h), \Delta O_3(h+1))$ (i.e.
427 the correlation between $\Delta O_3(h)$ and $\Delta O_3(h+1)$) is -0.45 , while the $corr(\Delta O_3(h), \Delta O_3(h+24))$ -0.68 , for any given
428 hour h . Similarly for EU, $corr(\Delta O_3(h)$ and $\Delta O_3(h+1))$ ranges between 0.31 (EU2) and 0.54 (EU3), while
429 $corr(\Delta O_3(h), \Delta O_3(h+24))$ -0.70 for all sub-regions. Thus, the ozone error with a 24h periodicity has a longer
430 memory than the error with a one hour periodicity. Since the 24h periodicity of the error is present in the
431 entire annual time series, the periodic error is not associated with particular conditions (e.g. stability), but is
432 rather embedded into the model at a more fundamental level. Moreover, similar periodicity is observed for
433 the ACF of ΔWS and $\Delta Temp$ for both models (not shown), reinforcing the notion that a daily process affecting
434 several model modules is not properly parameterised. As discussed in section 3.1, the representation of latent
435 and sensible heat fluxes in the version of CMAQ used in this study, (i.e. the errors in the timing of the PBL
436 collapse that has been addressed in a newer release of CMAQ) is likely (at least partially) responsible for the
437 daily periodic error noted here. Also for Chimere the reason for the error periodicity likely lies in the PBL
438 dynamics.

439 By removing the diurnal fluctuations (i.e. by screening out the frequencies between 12 hours and up to ~1.5
440 days by means of the Kolmogorov-Zurbenko (Kz) filter, as described in Hogrefe et al., 2000) from the modelled



441 and observed time series, the daily structure of the ACF disappears (**Figure 15b** and **Figure 16b**), replaced by a
442 slow decay and negative (EU1, EU2 and partially NA1, NA2) or fluctuating (NA3, EU3) correlation values. The
443 PACF plots in **Figure 15b** and **Figure 16b** suggest that some significant correlation persists up to ~40 hours,
444 likely due to leakage from the removed diurnal component (as extensively discussed in several earlier works,
445 the *kz* filter does not allow for a clear separation among components and thus some leakage is expected, see
446 e.g. Solazzo et al. 2017).

447 The relative strength of the MSE for the undecomposed ozone time series and for the ozone time series with
448 the diurnal fluctuations removed and with only the diurnal fluctuations is reported in Table 1. With the
449 exception of NA1 and EU3, the base line error (denoted with 'noDU') accounts for ~70 to 85% of the total
450 error, while the diurnal fluctuations (denoted with 'DU') are responsible for 10 to 23% of the total error (and
451 even less during nighttime). The 'DU' error outweighs the 'noDU' error (67% to 26%) only in EU3, where the
452 daily PBL issue has been pointed out in the previous section.

453 4.3 COVARIANCE ERROR: PHASE SHIFT OF THE DIURNAL CYCLE

454 This section explores the nature of the covariance error which occurs, among other reasons, when the two
455 signals being compared are not in phase. The first and second moments of the error distribution are invariant
456 with respect to a phase shift between the two signals (Murphy, 1995), i.e. the mean of the signal as well as the
457 amplitude of the oscillations with respect to the mean value are not affected by a phase shift which therefore
458 does not have an impact on the bias and variance components of the error. The correlation coefficient, on the
459 other hand, is impacted by a lagged signal, producing a net increase of the covariance error.

460 The analysis of the phase lag between the daily component of the modelled and observed cycles is reported in
461 **Figure 12** (NA) and **Figure 13** (EU), winter and summer are analysed separately.

462 To perform this analysis, the modelled and observed ozone time series are first filtered to isolate the diurnal
463 component using a *kz* filter. Then, the cross-covariance between the two time series is calculated. The time at
464 which the maximum covariance value occurs is taken as the phase shift between the two signals. The method
465 has an error of ± 0.5 hours.

466 In NA, the modelled diurnal peak occurs 1-2 hours earlier than the observed diurnal peak at many stations, and
467 up to 3-4 hours earlier at some Canadian stations. By taking into consideration the 0.5 hour error of the
468 estimate, the receptors at the western border (approximately corresponding to NA3) are least affected by this
469 timing error (especially in summer **Figure 12b**), and therefore the covariance share of the error shown in
470 **Figure 4** is not due to daily phase shift in this region but probably due to the shifting of longer (or shorter)
471 time periods induced for example by errors in transport (wind speed and/or direction). Figures S7 in the
472 Supplementary report the same analysis repeated for the 'zero Emi' and 'Zero BC' runs.

473 In the EU (**Figure 13**), no phase shift (or a phase shift compatible with the 0.5 hour estimation error) is
474 observed in Romania, Germany and the UK during winter, while a significant phase shift (the modelled peak
475 occurs up to 6 hours early) is observed in the North of Italy and Austria, with France and Spain oscillating
476 between positive 3 (model delay up to 5 hours in the south of Madrid) and negative 5 and 6 hour phase shifts,
477 with the net effect of a spatially aggregated daily cycle that is in phase with the observations (**Figure 3b**).
478 During summer the phase shift is larger and extends also to the countries where the phase shift was null
479 during winter. Moreover, some country-wise grouping can be detected, as for example at the border between
480 Belgium and France, Spain and France, Finland to Sweden, possibly due to the lack of harmonisation in the
481 timing of the reporting of observational values among EU countries (e.g. Solazzo and Galmarini, 2015).
482 Figures S8 in the Supplementary report the same analysis repeated for the 'zero Emi' and 'Const BC' runs.

483 While errors in emission profiles obviously can be one cause of the phase shift and thus the covariance error of
484 the modelled ozone signal, the representation of boundary layer processes clearly can be a factor as well. As



485 discussed in e.g. Herwehe et al. (2011), the parameterisation of vertical mixing during transitional periods of
486 the day can cause a time shift in the modelled ozone concentrations due to its effects on the near-surface
487 concentrations of NO_x and ozone, which in turn affect the chemical regime and balance between ozone
488 formation and removal.

489 To quantify the importance of the covariance error caused by a phase shift relative to other sources of error,
490 **Figure 14** shows the curves of normalised MSE as the observed ozone time series is shifted with respect to
491 itself between -10 and 10 hours. The MSE curve equals zero for a zero-hour lag and is symmetric with respect
492 to the sign of the lag. Since this analysis compares the observed signal to itself (with varying degrees of time
493 lags), the MSE fraction of bias and variance is zero while all of the MSE is due to the covariance.

494 The curves in **Figure 14** shows that a phase lag in the diurnal cycle of ±6 hour causes a MSE error in the diurnal
495 component of magnitude $\sim var(obs)$ (in both EU and NA), where $var(obs)$ is the variance of the measured
496 diurnal cycle (top panel). The effect on the full (undecomposed) time series is that a phase lag of ±4 (EU) and
497 ±5-6 (NA) hour in the diurnal cycle causes a MSE error of magnitude $\sim var(obs)$, where in this case the variance
498 is that of the undecomposed time series of ozone (lower panel).

499 Therefore, a modelled ozone peak that occurs 4 to 5 hours too early (a feature that is detected at some EU3
500 and Canadian stations) corresponds to a covariance error of 9.0 ppb (i.e. the standard deviation of the
501 network-average ozone observations in summer in both EU and NA). This result also helps explain the large
502 covariance error in EU3, which can be at least partially attributed to the large phase shift of the daily cycle.

503 4.4 EXPLAINING THE ERROR OF OZONE

504 In this section a simple linear regression model for the error of ozone ΔO_3 is applied with the goal of detecting
505 the causes of model errors on the daily and longer term scales identified in the previous section. Although a
506 linear model is overly simplistic and other methods are available (e.g kernel smoothers), we employed the
507 simpler approach since *i)* it is not the aim of this study to build a statistically accurate model for the model
508 error, and *ii)* by pursuing simple reasoning we hope to identify the time scale of the error and the most likely
509 fields causing it at that time scale. More advanced techniques are likely to overcomplicate the results and their
510 interpretations but could be pursued in future studies.

511 The available regressors (explanatory variables) are the errors of the variables for which measurements have
512 been collected within AQMEII, i.e. NO (EU only), NO₂, Temp, and WS:

$$\Delta O_3 = \beta_1 \Delta NO + \beta_2 \Delta NO_2 + \beta_3 \Delta Temp + \beta_4 \Delta WS + k \quad \text{Eq 3}$$

513

514 where β_i are the coefficients of the multiple linear regression, and the intercept k is the portion of the ozone
515 error not explainable by any of the regressors (the intercept). A bootstrap analysis (Mudelsee, 2014;
516 Groemping, 2006) is used to calculate the relative importance of each error field in explaining the variance of
517 ΔO_3 (**Figure 17** and **Figure 18**) with an uncertainty of ~5%. Since the measurements of ozone and NO_x are not
518 always co-located with the measurements of wind speed and temperature, **Eq 3** is strictly meaningful only in a
519 spatially-averaged sense.

520 None of the regressors help explain the winter ozone error of CMAQ, while ~15-20% of the ozone error
521 variability during summer is associated with the error in temperature and, to a lesser extent, wind speed. In
522 contrast, in Chimere the NO₂ error over EU during winter is highly correlated with the error of ozone, as is the
523 daytime wind speed error during summer (EU1 and EU2, **Figure 16a,b**). Overall, there is no instance where the
524 variance explained by the available variables (quantified through the coefficient of determination R^2) exceeds
525 0.60. There is an overwhelming daily memory of the error that can only partially be attributed to errors of the



526 available regressor variables, pointing to the need to include additional variables in future applications of this
527 regression analysis.

528 A straightforward limitation of Eq 3 is that it assumes that successive values of the error terms are independent
529 while in practice this is not the case (Table 2 reports the correlation coefficient of the diurnal fluctuations of
530 the residuals, obtained by filtering out fluctuations outside faster than ~1.5 days from the measured and
531 observed time series). Several significant collinearities can be detected (e.g. between ΔWS and $\Delta Temp$; ΔNO_2
532 and $\Delta Temp$, especially in winter).

533 In addition to the collinearity issue, there are other endogenous variables whose error contributes to total ΔO_3
534 that are not part of the regression analysis, as revealed by the ACF and PACF of the first-order differentiated
535 residuals of the regression in the last panels of each plot. Such missing variables are likely to correlate with
536 both the dependent (ΔO_3) and the explanatory variables, an issue known as Omitted Variable Bias, e.g. Greene
537 (1993). For instance, errors in the cloud cover and/or radiation scheme, land use masking, etc. are shared by
538 the chemical species (ozone and its precursors) as well as by the meteorological fields. The ACF and PACF
539 suggest that the common, omitted error of the fit propagates with daily recurrence and is not explained by the
540 available variables, stressing the findings of the previous section and again pointing to PBL-related errors.

541 However, since we are not in a position to estimate the errors associated with PBL variables (radiation,
542 temperature, turbulence) an alternate approach is to filter out the diurnal process from the modelled and
543 observed time series and repeat the analysis based on Eq 3 (Figure S9 and Figure S10).

544 Table 3 reports the correlation coefficients of the residuals with the diurnal component filtered-out, and
545 indeed the collinearity has been largely removed, especially for NA, while for EU some strong correlation
546 persists (ΔNO_2 and ΔNO , and between ΔWS and $\Delta Temp$ in winter):

547 The R^2 of the regression for the 'no-DU' case drops drastically in summer (EU3 and all sub-regions in NA) as
548 shown in Figures S9 and S10. Moreover, this analysis and its comparison to the results presented in earlier
549 sections lead to the following conclusions:

- 550 • A strong daily error component is common to all variables investigated here.
- 551 • This error manifests itself in the correlation coefficient, thus is due to a variance/covariance type of
552 error (otherwise, if it was a bias-type error, the R^2 would have been similar between the analysis of
553 the signal with and without the diurnal component);
- 554 • At least in NA, the bias error discussed in section 3 cannot be explained simply in terms of the fields
555 NO_2 , Temp, and WS. Hence, the bias of the CMAQ model over the NA continent appears to be
556 associated with processes with longer time scales, such as boundary conditions (inducing mostly bias
557 error, as discussed in section 3), deposition, and/or transport (potential systematic errors in wind
558 direction, for example, would likely produce a bias-type error);
- 559 • For EU1 and EU2, the error in the meteorological fields (Temp and WS) seems to explain
560 approximately half of the summer ozone error, with a memory of up to 3-4 days (significant, although
561 small PACF values);
- 562 • For EU3, the large error identified in section 2 and 3 is indeed dominated by daily processes. The
563 RMSE of the observed vs modelled time series filtered to remove fluctuations faster than ~1.5 days is
564 ~46% of the RMSE of the unfiltered time series (4.2 ppb vs 8.8 ppb, daylight summer, rural stations
565 only). Daily variables (e.g. meteorological variables determining the heat fluxes such as temperature,
566 radiation) and/or precursor emission are likely responsible for the error.
- 567 • The impact of ΔNO_2 and ΔNO in EU (all sub-regions, mostly daylight) and of ΔWS in EU1 (and partially
568 EU2) on the error of ozone is similar with and without the diurnal fluctuations, indicating cross-
569 correlation of these error fields for periods longer than one day.



570 5. CONCLUSIONS

571 This study is part of the goal of AQMEII to promote innovative insights into the evaluation of regional air
572 quality models. This study is primarily meant to introduce evaluation methods that are innovative and that
573 move towards diagnosing the causes of model error. It focuses on the diagnostic of the error produced by
574 CMAQ and Chimere applied to calculate hourly surface ozone mixing ratios over North America and Europe.

575 We argue that the current, widespread practice (although with several exceptions) of using time-aggregate
576 metrics to merely quantify the average distance (in a metric space) between models and observations has
577 clear limitations and does not help target the causes of model error. We therefore propose to move towards
578 the qualification of the error components (bias, variance, covariance) and to assess each of them with relevant
579 diagnostic methods. At the core of the diagnostic methods we have devised over the years within AQMEII is
580 the quality of the information that can be extracted from model and measurements to aid understanding of
581 the causes of model error, thus providing more useful information to model developers and users than can be
582 gained from more aggregate metric. Applying such approaches on a routine basis would help boost the
583 confidence in using models prediction for various applications.

584 While remarking that the analyses carried out are not meant to compare the two models but are rather meant
585 to show how the two models, applied to different areas and using different emissions, respond to changes, the
586 main conclusions of this study are:

- 587 - While the zeroing/modification of input of ozone from the lateral boundaries causes a shift of the
588 ozone diurnal cycle in both CMAQ and Chimere, the response of the two models to a modification of
589 anthropogenic emission and deposition fluxes is very different. For CMAQ, the effect of removing
590 anthropogenic emissions causes a shift and a flattening of the diurnal curve (bias and variance error),
591 while for Chimere the effect is restricted to a shift. In contrast, setting the ozone dry deposition
592 velocity to zero causes a shift (bias error) for CMAQ, while a profound change of the error structure
593 occurs for Chimere with significant impacts not only on the bias but also the variance and covariance
594 terms.
- 595 - On a continent wide network-average, removing anthropogenic emissions causes an error increase of
596 45% (25%) during summer and of 56% (null) during winter for Chimere (CMAQ), while a zeroing of
597 ozone transport across the lateral boundaries causes an error increase of 30% during summer and of
598 180% during winter (CMAQ).
- 599 - Fluctuations slower than ~1.5 days account for 70-85% of the total ozone quadratic error. The
600 partition of this error into bias, variance and covariance depends on season and region. In general,
601 the CMAQ model suffers mostly from bias error (model overestimation during summer and
602 underestimation during winter), while the Chimere model is rather 'centred' (i.e. almost unbiased)
603 but suffers high covariance error (associated with the timing of the signal, thus likely to synoptic
604 drivers)
- 605 - A recursive, systematic error with daily periodicity is detected in both models, responsible for 10-20%
606 of the quadratic total error. For CMAQ it is likely to be associated with the timing of daily transitions
607 in the PBL between stable and convective conditions. An indirect confirmation comes from results
608 reported for a more recent version of CMAQ (Appel et al., 2016) which show a delay in the evening
609 collapse of the modelled PBL that is in better agreement with observations;
- 610 - The modelled ozone daily peak accurately reproduces the observed one, although with significant
611 exceptions in France, Italy and Austria for Chimere and with the exceptions of Canada and some areas
612 in the eastern US for CMAQ. In these regions the peak is anticipated by up to 6 hours, causing a
613 covariance error as large as 9 ppb;
- 614 - The ozone error in CMAQ has a weak/negligible dependence on the error of NO₂ and wind speed,
615 while the error of NO₂ impacts significantly the ozone error produced by Chimere. On time scales
616 longer than 1.5 days, the Chimere ozone error is significantly associated with the error in wind speed
617 in continental Europe and the error in temperature in the Atlantic region (the UK, western France and
618 northern Spain).



619 Although having exploited several evaluation frameworks over the past ten years within AQMEII (operational,
620 diagnostic, and probabilistic) the goal of clearly associating errors to processes has not yet been achieved. As
621 already suggested in the conclusions of the collective analysis of the AQMEII3 suite of model runs summarised
622 by Solazzo et al. (2017), future model evaluation activities would benefit from incorporating sensitivity
623 simulations and process specific analyses that help to disentangle the non-linearity of the many model
624 variables, possibly by focusing on smaller modelling communities. The ‘theory of evaluation’ being put forward
625 by the hydrology modelling community (Nearing et al., 2016 and references therein) may provide a template
626 for the air quality community to further advance their model evaluation approaches.

627

628 ACKNOWLEDGMENTS

629 We gratefully acknowledge the contribution of various groups to the third air Quality Model Evaluation
630 International Initiative (AQMEII) activity. The following agencies have prepared the data sets used in this
631 study: U.S. EPA (North American emissions processing and gridded meteorology); U.S. EPA, Environment
632 Canada, Mexican Secretariat of the Environment and Natural Resources (Secretaría de Medio Ambiente y
633 Recursos Naturales-SEMARNAT) and National Institute of Ecology (Instituto Nacional de Ecología-INE) (North
634 American national emissions inventories); TNO (European emissions processing); ECMWF/MACC (Chemical
635 boundary conditions). Ambient North American concentration measurements were extracted from
636 Environment Canada’s National Atmospheric Chemistry Database (NAtChem) PM database and provided by
637 several U.S. and Canadian agencies (AQS, CAPMoN, CASTNet, IMPROVE, NAPS, SEARCH and STN networks);
638 North American precipitation-chemistry measurements were extracted from NAtChem’s precipitation-
639 chemistry data base and were provided by several U.S. and Canadian agencies (CAPMoN, NADP, NBPMM,
640 NSPSN, and REPQ networks); the WMO World Ozone and Ultraviolet Data Centre (WOUDC) and its data-
641 contributing agencies provided North American and European ozonesonde profiles; NASA’s AEROSOL ROBOTIC
642 NETWORK (AeroNet) and its data-contributing agencies provided North American and European AOD
643 measurements; the MOZAIC Data Centre and its contributing airlines provided North American and European
644 aircraft takeoff and landing vertical profiles; for European air quality data the following data centers were used:
645 EMEP/EBAS and European Environment Agency/European Topic Center on Air and Climate Change/Air Quality
646 e-reporting provided European air- and precipitation-chemistry data. The Finnish Meteorological Institute for
647 providing biomass burning emission data for Europe. Data from meteorological station monitoring networks
648 were provided by NOAA and Environment Canada (for the US and Canadian meteorological network data) and
649 the National Center for Atmospheric Research (NCAR) data support section. Joint Research Center
650 Ispra/Institute for Environment and Sustainability provided its ENSEMBLE system for model output
651 harmonisation and analyses and evaluation. Although this work has been reviewed and approved for
652 publication by the U.S. Environmental Protection Agency, it does not necessarily reflect the views and policies
653 of the agency.

654 APPENDIX 1

655 The autocorrelation function (ACF) is derived by the autocovariance (ACV) and expresses the correlation of a
656 time series with its lagged version (e.g. Chatfield, 2004):

$$657 \quad ACV(k) = E\{[X(t) - \mu][X(t+k) - \mu]\} = Cov[X(t), X(t+k)];$$

$$658 \quad ACF(k) = ACV(k) / ACV(0)$$

659 At any lag k , the autocovariance coefficients c_k are given by:

$$c_k = \frac{1}{N} \sum_{t=1}^{N-k} (x_t - \bar{x})(x_{t+k} - \bar{x})$$



- 660 And, as usual, the autocorrelation coefficients are given by normalizing c_k with c_0 .
- 661 The partial autocorrelation function (PACF) measures the excess of correlation between two elements of $X(t)$
 662 lagged by s elements not accounted for by the autocorrelation of the intermediate $s-1$ elements. In other
 663 words, the ACF of $X(t)$ and $X(t+s)$ includes all the linear dependence between the intermediate $s-1$ lags. The
 664 PACF allows to investigate the direct effect of lag t on the lag $t+s$.
- 665 The advantage of using ACF and PACF is that are function of the lag k only (and not of the specific time t). This
 666 condition holds only if $X(t)$ is stationary (i.e. its mean and variance do not change over time). Several tests are
 667 available to check $X(t)$ for stationarity (e.g. Chatfield, 2004). Differencing the time series is typically a way to
 668 achieve stationarity.
- 669 REFERENCES
- 670 Appel, K. W., Chemel, C., Roselle, S. J., Francis, X. V., Hu, R.-M., Sokhi, R. S., Rao, S. T., and Galmarini, S.:
 671 Examination of the Community Multiscale Air Quality (CMAQ) model performance for North America and
 672 Europe for the AQMEII project, *Atmos. Environ.*, 53, 142–155, 2012.
- 673 Appel, K. W., Napelenok, S. L., Foley, K. M., Pye, H. O. T., Hogrefe, C., Luecken, D. J., Bash, J. O., Roselle, S. J.,
 674 Pleim, J. E., Foroutan, H., Hutzell, W. T., Pouliot, G. A., Sarwar, G., Fahey, K. M., Gantt, B., Gilliam, R. C.,
 675 Kang, D., Mathur, R., Schwede, D. B., Spero, T. L., Wong, D. C., and Young, J. O.: Overview and evaluation of
 676 the Community Multiscale Air Quality (CMAQ) model version 5.1, *Geosci. Model Dev. Discuss.*,
 677 doi:10.5194/gmd-2016-226, in review, 2016.
- 678 Bessagnet, B., Pirovano, G., Mircea, M., Cuvelier, C., Aulinger, A., Calori, G., Ciarelli, G., Manders, A., Stern, R.,
 679 Tsyro, S., García Vivanco, M., Thunis, P., Pay, M.-T., Colette, A., Couvidat, F., Meleux, F., Rouil, L., Ung, A.,
 680 Aksoyoglu, S., Baldasano, J. M., Bieser, J., Briganti, G., Cappelletti, A., D'Isidoro, M., Finardi, S., Kranenburg,
 681 R., Silibello, C., Carnevale, C., Aas, W., Dupont, J.-C., Fagerli, H., Gonzalez, L., Menut, L., Prévôt, A. S. H.,
 682 Roberts, P., and White, L.: Presentation of the EURODELTA III intercomparison exercise – evaluation of the
 683 chemistry transport models' performance on criteria pollutants and joint analysis with meteorology,
 684 *Atmos. Chem. Phys.*, 16, 12667–12701, doi:10.5194/acp-16-12667-2016, 2016.
- 685 Bonasoni, P., Evangelisti, F., Bonafe, U., Ravegnani, F., Calzolari, F., Stohl, A., Tositti, L., Tubertini, O.,
 686 Colombo, T., 2000. Stratospheric ozone intrusion episodes recorded at Mt. Cimone during the VOLTALP
 687 project: case studies. *Atmospheric Environment*, 34, 1355–1365.
- 688 Byun, D.W., Schere, (2006). Review of the governing equations, computational algorithms, and other
 689 components of the Models-3 community Multiscale Air Quality (CMAQ) modelling system. *Applied*
 690 *Mechanics Reviews*. v59 i2, 51–77
- 691 Camalier, L., Cox, W., Dolwick, P., 2007. The effects of meteorology on ozone in urban areas and their use in
 692 assessing ozone trends, *Atmospheric Environment*, Volume 41, Issue 33, October 2007, Pages 7127–7137,
 693 ISSN 1352-2310, <http://dx.doi.org/10.1016/j.atmosenv.2007.04.061>
- 694 Chatfield, C., 2004. *The analysis of time series. An introduction*. Sixth ed. s.l.:Chapman & Hall/CRC.
- 695 Dennis, R. et al., 2010. A framework for evaluating regional-scale numerical photochemical modelling systems.
 696 *Environ. Fluid Mech.*, Volume 10, pp. 471–489.
- 697 Entekhabi, D., Reichle, R. H., Koster, R. D. & Crow, W. T., 2010. Performance metrics for soil moisture retrievals
 698 and application requirements. *J.Hydrometeor*, Volume 11, pp. 832–840.
- 699 Galmarini, S., Koffi, B., Solazzo, E., Keating, T., Hogrefe, C., Schulz, M., Benedictow, A., Griesfeller, J.J., Janssens-
 700 Maenhout, G., Carmichael, G., Fu, J., Dentener, F., 2017. Harmonisation of the multi-scale multi-model
 701 activities HTAP, AQMEII and MICS-Asia: simulations, emission inventories, boundary conditions and output
 702 formats. *Atmospheric Chemistry and Physics*, in press
- 703 Greene, W. H., 1993. *Econometric Analysis*. Second ed. s.l.:Macmillan.
- 704 Groemping, U., 2006. Relative Importance for Linear Regression in R: The Package relaimpo. *Journal of*
 705 *Statistical Software*, 17(1).



- 706 Guenther, A. B., Jiang, X., Heald, C. L., Sakulyanontvittaya, T., Duhl, T., Emmons, L. K., and Wang, X.: The Model
707 of Emissions of Gases and Aerosols from Nature version 2.1 (MEGAN2.1): an extended and updated
708 framework for modelling biogenic emissions, *Geosci. Model Dev.*, 5, 1471-1492, doi:10.5194/gmd-5-1471-
709 2012, 2012
- 710 Gupta, H. V., Kling, H., Yilamz, K. K. & Martinez, G. F., 2009. Decomposition of the mean square error and NSE
711 performance criteria: implications for improving hydrological modelling. *Journal of Hydrology*, Volume 377,
712 pp. 80-91.
- 713 Gupta, H. V., Wagener, T. & Liu, Y., 2008. Reconciling theory with observations: elements of a diagnostic
714 approach to model evaluation. *Hydrological Processes*, Volume 22, pp. 3802-3813.
- 715 Herwehe, J. A., Otte, T. L., Mathur, R. & Rao, S. T., 2011. Diagnostic analysis of ozone concentrations simulated
716 by two regional-scale air quality models. *Atmospheric Environment*, Volume 45, pp. 5957-5969.
- 717 Hogrefe, C. et al., 2014. Space-time analysis of the Air Quality Model Evaluation International Initiative
718 (AQMEII) Phase 1 air quality simulations. *J Air Waste Manag Assoc*, 64(4), pp. 388-405.
- 719 Hogrefe, C., Rao, S. T., Zurbenko, I. G. & Porter, P. S., 2000. Interpreting the information in ozone observations
720 and model predictions relevant to regulatory policies in the Eastern United States. *B. Am. Meteorol. Soc.*,
721 Volume 81, pp. 2083-2106.
- 722 Im, U., Bianconi, R., Solazzo, E., Kioutsioukis, I., Badia, A., Balzarini, A., Baro, R., Bellasio, R., Brunner, D.,
723 Chemel, C., Curci, G., Denier van der Gon, H., Flemming, J., Forkel, R., Giordano, L., Jimenez-Guerrero, P.,
724 Hirtl, M., Hodzic, A., Honzak, L., Jorba, O., Knote, C., Makar, P. A., Manders-Groot, A., Neal, L., Pérez, J. L.,
725 Pirovano, G., Pouliot, G., San Jose, R., Savage, N., Schroder, W., Sokhi, R. S., Syrakov, D., Torian, A.,
726 Tuccella, P., Wang, K., Werhahn, J., Wolke, R., Zabkar, R., Zhang, Y., Zhang, J., Hogrefe, C., and Galmarini, S.:
727 Evaluation of operational online coupled regional air quality models over Europe and North America in the
728 context of AQMEII phase 2. Part II: particulate matter, *Atmos. Environ.*, 115, 421-441, 2015a.
- 729 Im, U., Bianconi, R., Solazzo, E., Kioutsioukis, I., Badia, A., Balzarini, A., Baro, R., Bellasio, R., Brunner, D.,
730 Chemel, C., Curci, G., Flemming, J., Forkel, R., Giordano, L., Jimenez-Guerrero, P., Hirtl, M., Hodzic, A.,
731 Honzak, L., Jorba, O., Knote, C., Kuenen, J. J. P., Makar, P. A., Manders-Groot, A., Neal, L., Pérez, J. L.,
732 Pirovano, G., Pouliot, G., San Jose, R., Savage, N., Schroder, W., Sokhi, R. S., Syrakov, D., Torian, A., Tuccella,
733 P., Werhahn, J., Wolke, R., Yahya, K., Zabkar, R., Zhang, Y., Zhang, J., Hogrefe, C., and Galmarini, S.: Evaluation
734 of operational online-coupled regional air quality models over Europe and North America in the context of
735 AQMEII phase 2. Part I: ozone, *Atmos. Environ.*, 115, 404-420, 2015b.
- 736 Kioutsioukis et al., 2016; Insights into the deterministic skill of air quality ensembles from the analysis of
737 AQMEII data. *Atmospheric Chemistry and Physics* 16(24):15629-15652
- 738 Lemaire, V.E.P., Colette, A., Menut, L., 2016. Using statistical models to explore ensemble uncertainty in
739 climate impact studies: the example of air pollution in Europe. *Atmos. Chem. Phys.*, 16, 2559-2574, 2016
740 doi:10.5194/acp-16-2559-2016
- 741 Lattuati M., 1997: Impact des émissions européennes sur le bilan d'ozone troposphérique à l'interface de
742 l'Europe et de l'Atlantique Nord : apport de la modélisation lagrangienne et des mesures en altitude. Ph.D.
743 Thesis, Université Pierre et Marie Curie, Paris, France
- 744 Makar, P.A., Gong, W., Mooney, C., Zhang, J., Davignon, D., Samaali, M., Moran, M.D., He, H., Tarasick, D.W.,
745 Sills, D., and Chen, J., 2010. Dynamic adjustment of climatological ozone boundary conditions for Air-
746 Quality Forecasts, *Atmos. Chem. Phys.* 10 (6), 8997-9015
- 747 Menut, L., B. Bessagnet, D. Khvorostyanov, M. Beekman, N. Blond, A. Colette, I. Coll, G. Curci, G. Foret, A.
748 Hodzic, S. Mailler, F. Meleux, J.-L. Monge, I. Pison, G. Siour, S. Turquety, M. Valari, R. Vautard, and M.
749 G. Vivanco, 2013. CHIMERE 2013: a model for regional atmospheric composition modelling. *Geosci. Model*
750 *Dev.*, 6, 981-1028, 2013
- 751 Mudelsee, M., 2014. *Climate time series analysis*. second ed. s.l.:Springer.
- 752 Murphy, A. H., 1988. Skill scores based on the mean square error and their relationships to the correlation
753 coefficient. *Mon. Wae. Rev.*, Volume 116, pp. 2417-2424.



- 754 Murphy, A. H., 1993. What is a good forecast?: An essay on the nature of goodness in weather forecasting.
 755 *Weather Forecast*, Volume 8, pp. 281-293.
- 756 Murphy, A. H., 1995. The coefficient of correlation and determination as measures of performance in forecast
 757 verification. *Weather and Forecasting*, Volume 10, pp. 681-688.
- 758 Otero, N. et al., 2016. Synoptic and meteorological drivers of extreme ozone concentrations over Europe.
 759 *Environ. Res. Lett.*, Volume 11.
- 760 Nearing, G.S., Tian, Y., Gupta, H.V., Clark, M.P., Harrison, K.W., Wejs, V., 2016. A philosophical basis for
 761 hydrological uncertainty. *Hydrological Sciences Journal* 6(9), 1666-1678
- 762 Rao, S. T., Galmarini, S., and Puckett, K.: Air quality model evaluation international initiative (AQMEII), *B. Am.*
 763 *Meteorol. Soc.*, 92, 23–30, doi:10.1175/2010BAMS3069.1, 2011.
- 764 Simon, H., Baker, K. R. & Phillips, S., 2012. Compilation and interpretation of photochemical model
 765 performance statistics published between 2006 and 2012. *Atmospheric Environment*, Volume 61, pp. 124-
 766 139.
- 767 Skamarock, W. C., Klemp, J. B., Dudhia, J., Gill, D. O., Barker, D. M., Duda, M. G., Huang, X-Y, Wang, W., and
 768 Powers, J. G.: A description of the advanced research WRF version 3. NCAR Tech Note NCAR/TN 475 STR,
 769 125 pp, 2008.
- 770 Solazzo, E. & Galmarini, S., 2015. Comparing apples with apples: Using spatially distributed time series of
 771 monitoring data for model evaluation. *Atmos. Environ.*, Volume 112, pp. 234-245.
- 772 Solazzo, E. & Galmarini, S., 2016. Error Apportionment for atmospheric chemistry transport models: a new
 773 approach to model evaluation. *Atmospheric Chemistry and Physics*, Volume 16, pp. 6263-6283.
- 774 Solazzo, E. et al., 2017. Evaluation and error apportionment of an ensemble of atmospheric chemistry
 775 transport modelling systems: multi variable temporal and spatial breakdown. *Atmospheric Chemistry and*
 776 *Physics*.
- 777 Solazzo, E., Bianconi, R., Pirovano, G., Matthias, V., Vautard, R., Moran, M. D., Appel, K. W., Bessagnet, B.,
 778 Brandt, J., Christensen, J. H., Chemel, C., Coll, I., Ferreira, J., Forkel, R., Francis, X. V., Grell, G., Grossi, P.,
 779 Hansen, A. B., Hogrefe, C., Miranda, A. I., Nopmongco, U., Prank, M., Sartelet, K. N., Schaap, M., Silver, J. D.,
 780 Sokhi, R. S., Vira, J., Werhahn, J., Wolke, R., Yarwood, G., Zhang, J., Rao, S. T., and Galmarini, S.: Operational
 781 model evaluation for particulate matter in Europe and North America in the context of AQMEII, *Atmos.*
 782 *Environ.*, 53, 75–92, 2012b.
- 783 Solazzo, E., Bianconi, R., Pirovano, G., Moran, M. D., Vautard, R., Hogrefe, C., Appel, K. W., Matthias, V., Grossi,
 784 P., Bessagnet, B., Brandt, J., Chemel, C., Christensen, J. H., Forkel, R., Francis, X. V., Hansen, A. B., McKeen,
 785 S., Nopmongcol, U., Prank, M., Sartelet, K. N., Segers, A., Silver, J. D., Yarwood, G., Werhahn, J., Zhang, J.,
 786 Rao, S. T., and Galmarini, S.: Evaluating the capability of regional-scale air quality models to capture the
 787 vertical distribution of pollutants, *Geosci. Model Dev.*, 6, 791–818, doi:10.5194/gmd-6-791-2013, 2013
- 788 Solazzo, E., Bianconi, R., Vautard, R., Appel, K.W., Moran, M. D., Hogrefe, C., Bessagnet, B., Brandt, J.,
 789 Christensen, J. H., Chemel, C., Coll, I., van der Gon, H. D., Ferreira, J., Forkel, R., Francis, X. V., Grell, G.,
 790 Grossi, P., Hansen, A. B., Jericevic, A., Kraljevic, L., Miranda, A. I., Nopmongcol, U., Pirovano, G., Prank, M.,
 791 Riccio, A., Sartelet, K. N., Schaap, M., Silver, J. D., Sokhi, R. S., Vira, J., Werhahn, J., Wolke, R., Yarwood, G.,
 792 Zhang, J., Rao, S. T., and Galmarini, S.: Model evaluation and ensemble modelling of surface-level ozone in
 793 Europe and North America in the context of AQMEII, *Atmos. Environ.*, 53, 60–74, 2012a.
- 794 Steyn, D. G. & Galmarini, S., 2008. Evaluating the predictive and explanatory value of atmospheric numerical
 795 models: between relativism and objectivism. *The Open Atmospheric Science Journal*, Volume 2, pp. 38-45.
- 796 Theil, H., 1961. *economic forecast and policy*. Amsterdam: North-Holland.
- 797 Tian, Y. et al., 2016. performance metric, error modelling and uncertainty quantification. *American*
 798 *Meteorological Society*, Volume 144, pp. 607-613.
- 799 Torrence, C. & Compo, G. P., 1997. A Practical Guide to Wavelet Analysis. *Bulletin of the American*
 800 *Meteorological Society*, 79(1), pp. 61-78.



- 801 Vautard, R., Moran, M., Solazzo, E., Gilliam, R., Volker, M., Bianconi, R., and et al., 2012. Evaluation of the
 802 meteorological forcing used for the Air Quality Model Evaluation International Initiative (AQMEII) air
 803 quality simulations. *Atmospheric Environment* 53, 15-37
- 804 Wagener, T. & Gupta, H. V., 2005. Model identification for hydrological forecasting under uncertainty.
 805 *Stochastic Environmental Research*, 19(6), pp. 378-387.
- 806 Weijs, A. V., Schoups, G. & van de Giesen, N., 2010. why hidrological predictions should be evaluated using
 807 information theory. *Hydrol. Earth Syst. Sci.*, Volume 14, pp. 2545-2558.
- 808 Wilks, D. S., 2011. *Statistical methods in atmospheric sciences*. s.l.:Academic Press.
- 809 Wilmott, C. J., 1981. On the validation of models. *Phys Geogr*, Volume 2, pp. 184-194.
- 810 Whitten, G.Z., Heo, G., Kimura, Y., McDonald-Buller, E., Allen, D.T., Carter, W.P.L., and Yarwood, G.: A new
 811 condensed toluene mechanism for Carbon Bond: CB05-TU. *Atmospheric Environment* 44, 5346-5355, 2010.

812 TABLES

813 **TABLE 1.** MSE (ppb²) of the full, undecomposed ozone time series (FT) and relative fraction of MSE of the time series derived by filtering
 814 out the diurnal fluctuations (noDU) and of the time series derived by keeping only the diurnal fluctuations (DU). The diurnal signal has
 815 been isolated by applying a filter kz(13,5). The relative fraction of noDU and of DU not adding up to 100% is because the filter allows some
 816 leakage to the nearest frequencies (see Hogrefe et al. (2000) and Solazzo and Galmarini (2016) for details). a) NA; b) EU

817 a)

NA1			NA2			NA3		
CMAQ MSE- Summer								
FT (ppb ²)	noDU	DU	FT (ppb ²)	noDU	DU	FT (ppb ²)	noDU	DU
28.65	40%	41%	49.12	70%	23%	79.35	84%	13%
CAMQ MSE- Winter								
86.08	94%	5%	19.27	75%	21%	61.67	74%	21%

818

819 b)

EU1			EU2			EU3		
CHIMERE MSE- Summer								
FT (ppb ²)	noDU	DU	FT (ppb ²)	noDU	DU	FT (ppb ²)	noDU	DU
20.91	85%	10%	46.19	78%	15%	125.86	26%	67%
CHIMERE MSE- Winter								
20.87	85%	12%	19.95	85%	10%	39.91	38%	59%

820

821 **TABLE 2.** Linear correlation coefficient between the diurnal residuals of the regressors of Eq 3. The residuals are calculated by removing
 822 from the measured and modelled time series fluctuations faster the -1.5 days. All the correlation values are significant up to 1%
 823 significance threshold. a) NA; b) EU

824 a)

	Correlation among diurnal component of residuals								
	ΔNO_2			ΔTemp			ΔWS		
	NA1	NA2	NA3	NA1	NA2	NA3	NA1	NA2	NA3
SUMMER									
ΔNO_2	1	0.6	0.65	0.6	0.23	0.65	-0.19	0.46	-0.26
ΔTemp	-0.6	1	0.65	1	0.62	0.7	0.62	0.53	0.7
ΔWS	-0.19	0.46	-0.26	0.62	0.53	0.7	1	1	1
WINTER									
ΔNO_2	1	0.63	0.56	0.63	0.57	0.56	-0.55	-0.05	-0.19
ΔTemp	-0.63	1	0.56	1	0.63	0.35	0.63	0.47	0.35
ΔWS	-0.55	-0.05	-0.19	0.49	0.47	0.35	1	1	1

825

826 b)



827
 828

	Correlation among diurnal component of residuals											
	ΔNO			ΔNO_2			ΔTemp			ΔWS		
	EU1	EU2	EU3	EU1	EU2	EU3	EU1	EU2	EU3	EU1	EU2	EU3
	SUMMER											
ΔNO	1	1	1	0.05	0.68	0.48	-0.08	-0.05	-0.27	-0.07	0.11	-0.02
ΔNO_2	0.05	0.68	0.48	1	1	1	0.57	0.18	-0.27	0.51	0.38	0.26
ΔTemp	-0.08	-0.05	-0.27	0.57	0.18	-0.27	1	1	1	0.81	0.63	0.21
ΔWS	-0.07	0.11	-0.02	0.51	0.38	0.26	0.81	0.63	0.21	1	1	1
	WINTER											
ΔNO	1	1	1	0.31	0.6	0.73	0.02	-0.52	-0.62	0.03	0.12	0.06
ΔNO_2	0.31	0.6	0.73	1	1	1	0.13	-0.7	-0.7	-0.01	0.09	0.11
ΔTemp	0.02	-0.52	-0.62	0.13	-0.7	-0.7	1	1	1	0.48	0.02	-0.01
ΔWS	0.03	0.12	0.06	-0.01	0.09	0.11	0.48	0.02	-0.01	1	1	1

829 **TABLE 3.** Linear correlation coefficient between the residuals of the regressors of Eq 3, when the diurnal fluctuations are filtered out. The
 830 residuals are calculated by removing from the measured and modelled time series fluctuations faster than ~ 1.5 days. All the correlation
 831 values are significant up to 1% significance threshold. a) NA; b) EU

832 a)

833

	Correlation among residuals (diurnal fluctuations removed)								
	ΔNO_2			ΔTemp			ΔWS		
	NA1	NA2	NA3	NA1	NA2	NA3	NA1	NA2	NA3
	SUMMER								
ΔNO_2	1	1	1	-0.2	-0.02	-0.26	-0.06	-0.05	-0.19
ΔTemp	-0.2	-0.02	-0.26	1	1	1	0.28	0.09	0.42
ΔWS	-0.06	-0.05	-0.19	0.28	0.09	0.42	1	1	1
	WINTER								
ΔNO_2	1	1	1	-0.12	-0.42	-0.03	-0.02	-0.16	-0.11
ΔTemp	-0.12	-0.42	-0.03	1	1	1	0.54	0.34	0.13
ΔWS	-0.02	-0.16	-0.11	0.54	0.34	0.13	1	1	1

834 b)

835

	Correlation among residuals (diurnal fluctuations removed)											
	ΔNO			ΔNO_2			ΔTemp			ΔWS		
	EU1	EU2	EU3	EU1	EU2	EU3	EU1	EU2	EU3	EU1	EU2	EU3
	SUMMER											
ΔNO	1	1	1	0.22	0.71	0.69	0.12	0.23	-0.03	0.06	0.23	0.08
ΔNO_2	0.22	0.71	0.69	1	1	1	0.27	0.41	0.11	0.54	0.43	0.01
ΔTemp	0.12	0.23	0.03	0.27	0.41	0.11	1	1	1	0.44	0.22	0.36
ΔWS	0.06	0.23	0.08	0.54	0.43	0.01	0.44	0.22	0.36	1	1	1
	WINTER											
ΔNO	1	1	1	0.21	0.64	0.46	-0.22	-0.19	-0.02	-0.15	-0.14	-0.01
ΔNO_2	0.21	0.64	0.46	1	1	1	-0.09	-0.38	-0.35	-0.07	-0.2	-0.08
ΔTemp	-0.22	-0.19	-0.02	-0.09	-0.38	-0.35	1	1	1	0.37	-0.1	0.38
ΔWS	-0.15	-0.14	-0.01	-0.07	-0.2	-0.08	0.37	-0.1	0.38	1	1	1

836 **FIGURES**

837 **Figure 1** Continental domains and sub-regions used for analysis. The networks of ozone receptors are also
 838 shown.

839 **Figure 2.** Average monthly and diurnal curves constructed from January – December 2010 time series of hourly
 840 ozone observations and model simulations for three North American sub-regions

841 **Figure 3.** Average monthly and diurnal curves constructed from January – December 2010 time series of hourly
 842 ozone observations and model simulations for three European sub-regions.



843 **Figure 4** MSE decomposition for June – August hourly ozone into bias², variance and covariance for the three
844 NA sub-regions. Results are presented separately for daylight hours (left) and nighttime hours (right).

845 **Figure 5** MSE decomposition for June – August hourly ozone into bias², variance and covariance for the three
846 EU sub-regions (the zero_Dep data refers to the month of July only). Results are presented separately for
847 daylight hours (left) and nighttime hours (right)

848 **Figure 6** CMAQ MSE breakdown for summer and winter for the base case and sensitivity simulations over NA.
849 The error coefficients F_b, F_v, F_c are reported on the left axis, the total MSE (ppb^2) on the right axis (red triangles).
850 The '+' and '-' signs within the bias and variance portions of the errors indicate model over- or under-
851 prediction of mean concentration or variance, respectively. The values in the covariance portion indicate the
852 correlation coefficient between modelled and observed time series. *a)* hourly time series of ozone (base case);
853 *b)* hourly time series of '20% reduction' scenario; *c)* hourly time series of 'zero boundary conditions' scenario;
854 *d)* hourly time series of the 'zeroed anthropogenic emissions' scenario; *e)* base case rolling average daily
855 maximum 8-hour ozone time series. For the analysis of hourly time series in panels a) – d), results are provided
856 separately for daytime and nighttime.

857 **Figure 7.** Chimere MSE breakdown for summer and winter for the base case and sensitivity simulations over
858 EU. The error coefficients F_b, F_v, F_c are reported on the left axis, the total MSE (ppb^2) on the right axis (red
859 triangles). The '+' and '-' signs within the bias and variance portions of the errors indicate model over- or
860 under-prediction of mean concentration or variance, respectively. The values in the covariance portion
861 indicate the correlation coefficient between modelled and observed time series. *a)* hourly time series of ozone
862 (base case); *b)* hourly time series of '20% reduction' scenario; *c)* hourly time series of 'constant boundary
863 conditions' scenario; *d)* hourly time series of the 'zeroed anthropogenic emissions' scenario; *e)* base case
864 rolling average daily maximum 8-hour ozone time series. For the analysis of hourly time series in panels a) – d),
865 results are provided separately for daytime and nighttime.

866 **Figure 8.** Top row: Spatial maps of RMSE (in ppb) for the base case. Middle row: Percentage RMSE changes for
867 the zeroed emissions case with respect to the base case. Lower row: Percentage RMSE changes for the zeroed
868 boundary condition case with respect to the base case. Left column: Winter months (DJF); Right column:
869 summer months (JJA).

870 **Figure 9** Top row: Spatial maps of RMSE (in ppb) for the base case. Middle row: Percentage RMSE changes for
871 the zeroed emissions case with respect to the base case. Lower row: Percentage RMSE changes for the
872 constant boundary condition case with respect to the base case.. Left column: Winter months (DJF); Right
873 column: summer months (JJA).

874 **Figure 10.** Annual time series of differences between CMAQ and observed O_3 (ΔO_3 , top panel) and Morlet
875 wavelet analysis of the periodogram of ΔO_3 (lower panel) for the three NA subdomains. Black contours lines
876 identify the 95% confidence interval. The period (in days) is reported in the vertical axis, while the quantiles of
877 the power spectral density are measured in ppb^2 . (the scale reports the quantiles of the power spectrum).

878 **Figure 11.** Same as in FIGURE 10 for Chimere over the three EU subdomains

879 **Figure 12.** Phase shift of the diurnal cycle (in hours). A positive phase shift indicates that the model peak is
880 'late', while a negative phase shift indicates that the modelled peak precedes the observed peak. This analysis
881 includes urban and suburban stations in addition to rural stations.

882 **Figure 13.** As in Figure 12 for EU.

883 **Figure 14.** Normalised MSE produced by lagging the observed diurnal cycle with respect to itself. The MSE due
884 to such a shift is entirely due to covariance error. The plots are presented for EU2 (left) and NA2 (right) for the



885 months of JJA. The top panel shows the impact of the phase shift on the DU component, and the lower panels
886 show results for the undecomposed time series (FT). For EU2, a shift of ± 3 hours causes an MSE of ~ 0.5 times
887 the variance of the observations.

888 **Figure 15.** CMAQ model: autocorrelation (ACF) and partial autocorrelation (PACF) function for *a*) the
889 differenced time series of residuals of ozone (mod-obs) and *b*) the differenced time series of residual of ozone
890 obtained by filtering out the diurnal fluctuations from the modelled and observed time series. The
891 differentiation is necessary to remove non-stationarity.

892 **Figure 16.** Chimere model: autocorrelation (ACF) and partial autocorrelation (PACF) function for *a*) the
893 differenced time series of residuals of ozone (mod-obs) and *b*) the differenced time series of residual of ozone
894 obtained by filtering out the diurnal fluctuations from the modelled and observed time series. The
895 differentiation is necessary to remove non-stationarity.

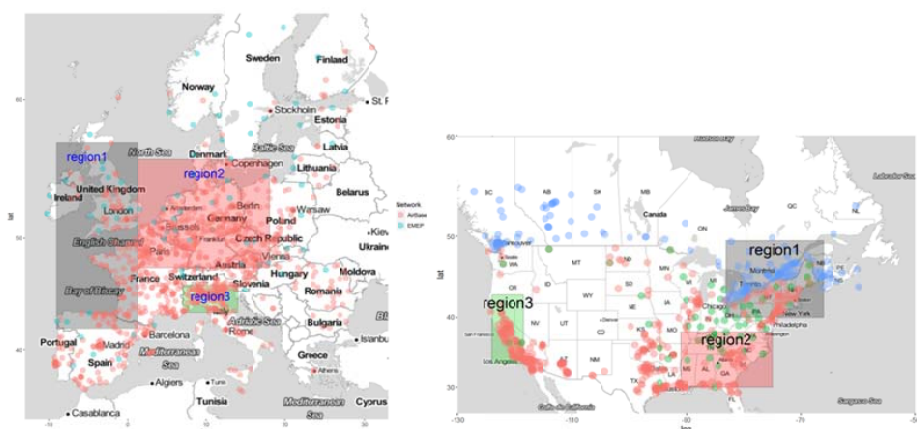
896 **Figure 17.** Percentage of variance explained by the regressors (the total R^2 for the regression is reported in the
897 title of each panel). The relative importance of each variable is assessed by using a bootstrap resampling. The
898 plots at the bottom show the ACF and PACF of the yearly time series of residual of the fit, i.e. the portion of
899 the ozone time series that was not captured by the linear regressions on the available variables.

900 **Figure 18.** Same as **Figure 17** for EU.

901

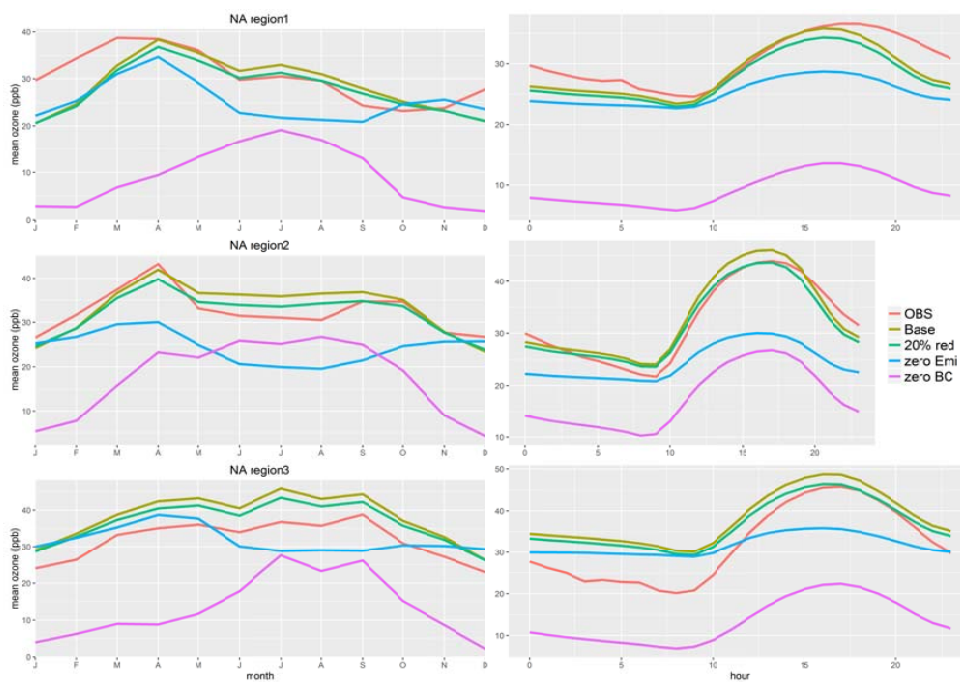


905 FIGURES



906

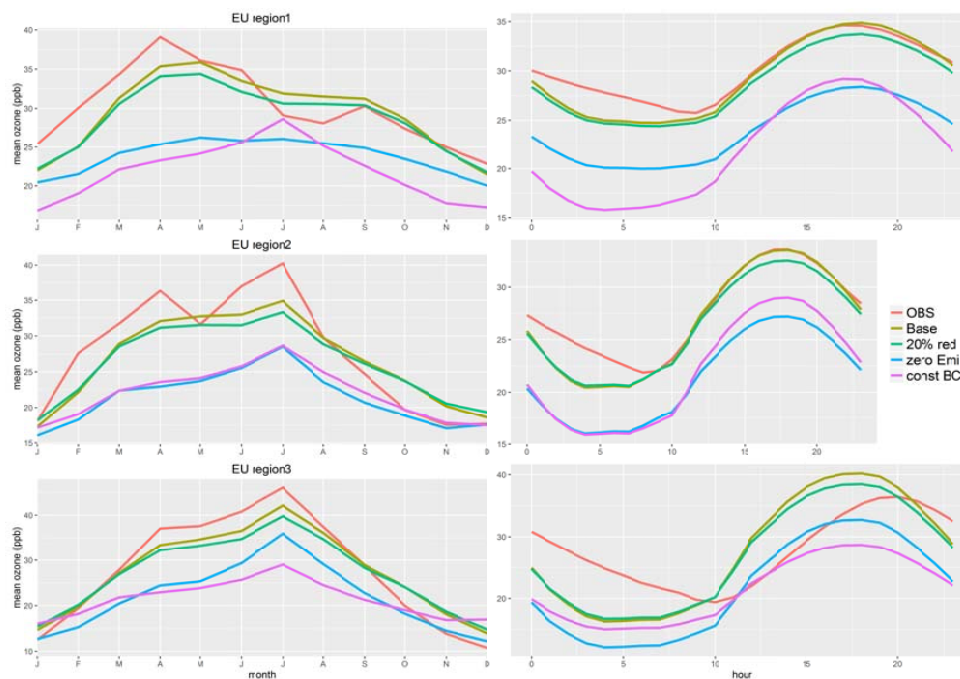
907 **FIGURE 1.** Continental domains and sub-regions used for analysis. The networks of ozone receptors are also shown



908

909

913 **FIGURE 2.** Average monthly and diurnal curves constructed from January – December 2010 time series of hourly ozone observations and
 914 model simulations for three North American sub-regions.



915
916

917 **FIGURE 3.** Average monthly and diurnal curves constructed from January – December 2010 time series of hourly ozone observations and
918 model simulations for three European sub-regions.

916

917

918

919

920

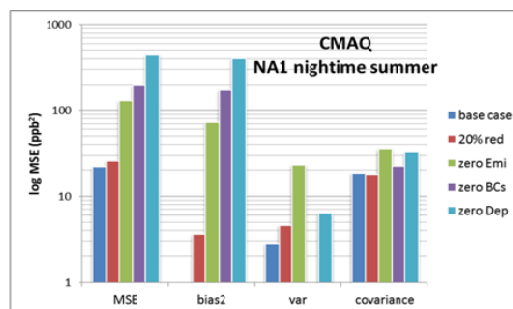
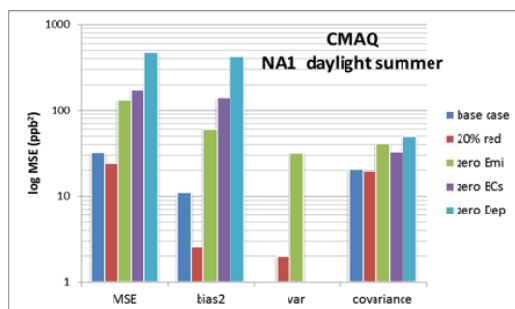
921

922

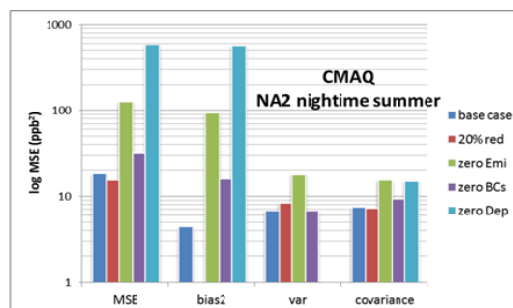
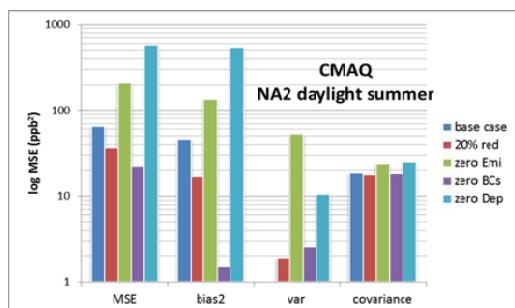
923



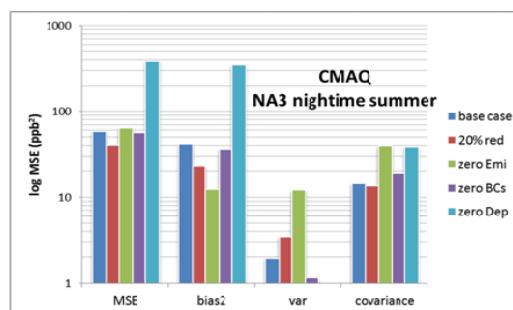
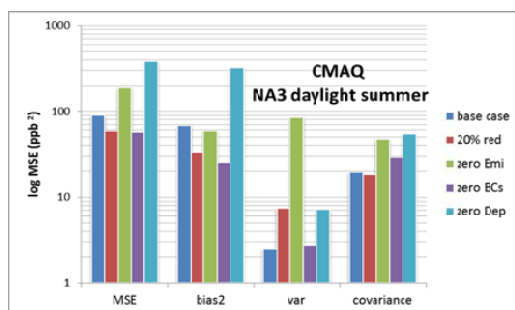
924



925



926



927

931 **FIGURE 4.** MSE decomposition for June – August hourly ozone into bias², variance and covariance for the three NA sub-regions. Results are
 932 presented separately for daylight hours (left) and night-time hours (right)

930

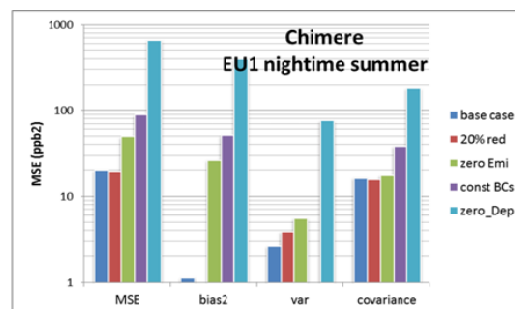
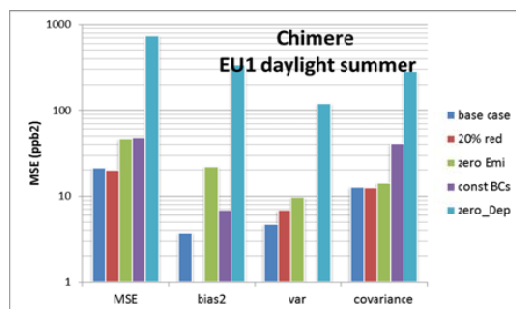
931

932

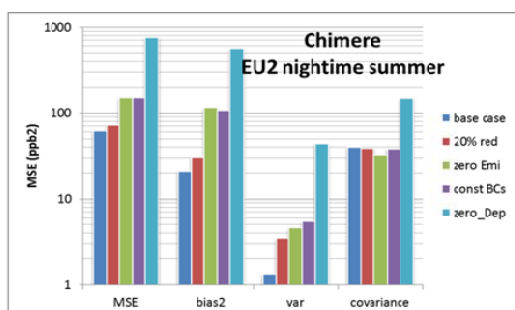
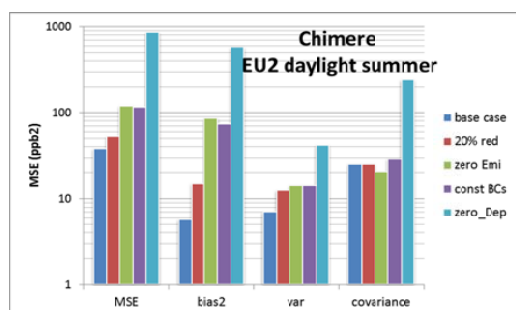
933



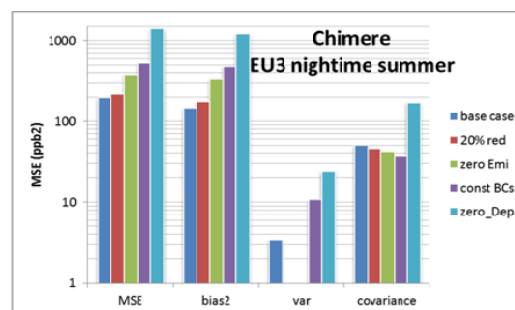
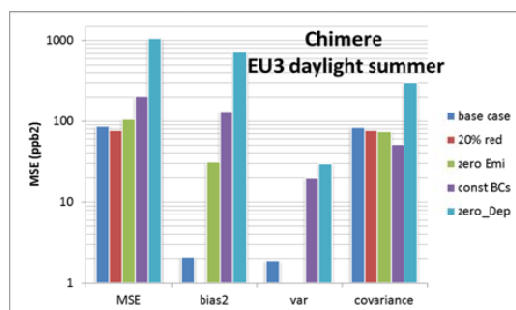
934



935

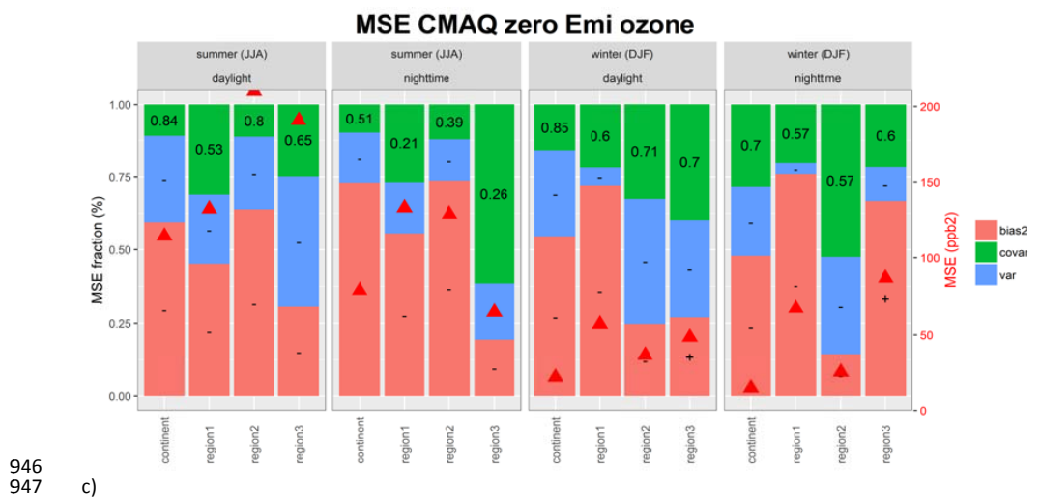
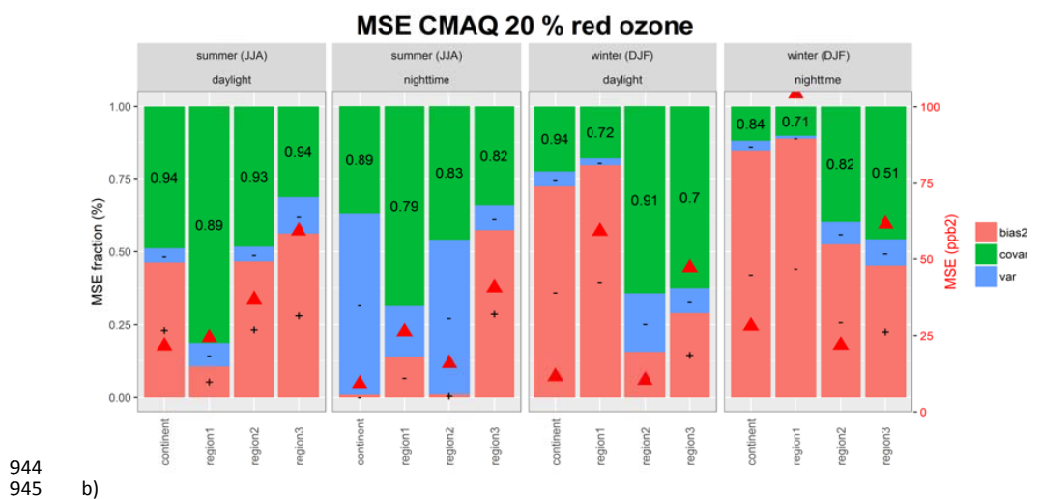
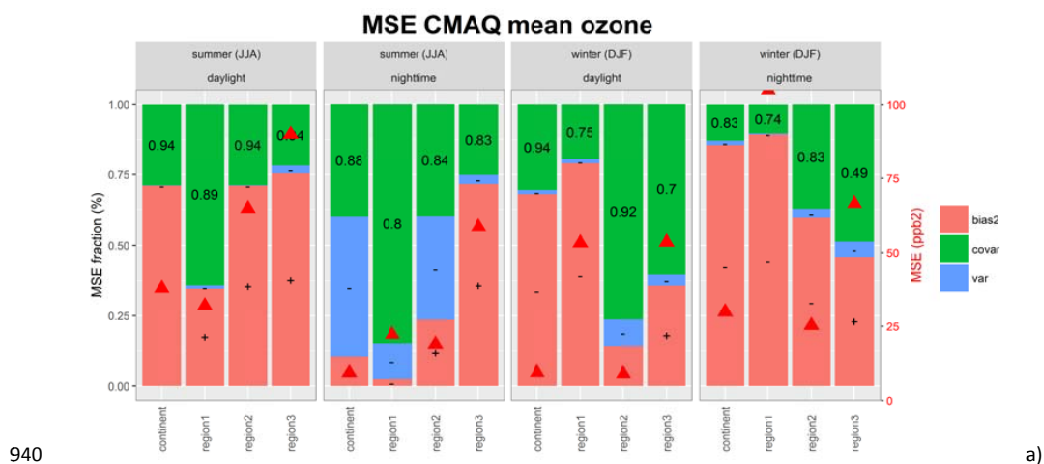


936



940 **FIGURE 5.** MSE decomposition for June – August hourly ozone into bias², variance and covariance for the three EU sub-regions (the
 941 zero_Dep data refers to the month of July only). Results are presented separately for daylight hours (left) and night-time hours (right)

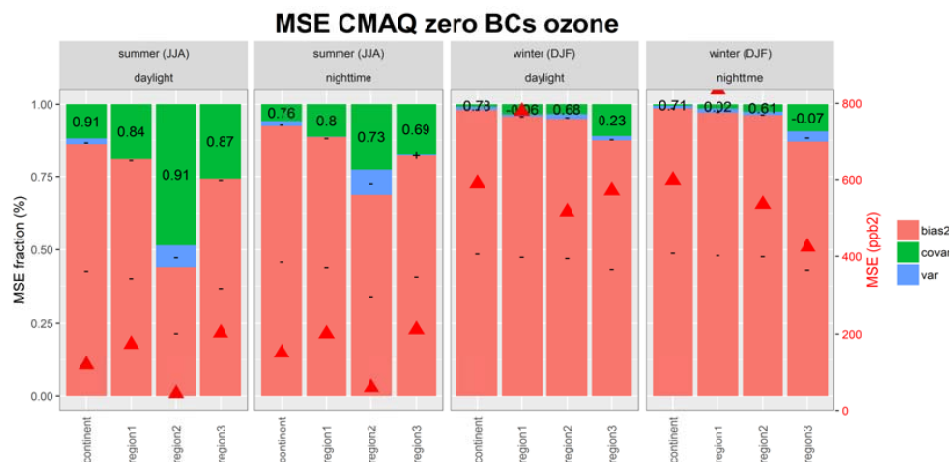
939



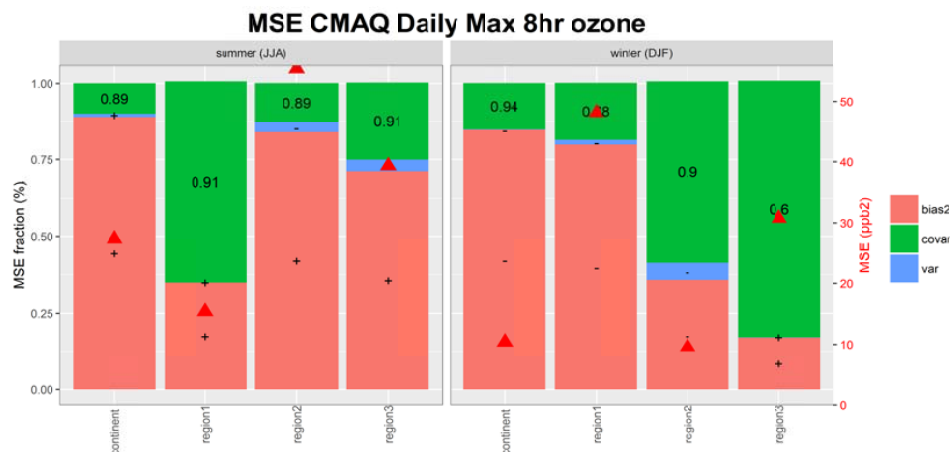


948
 949

d)



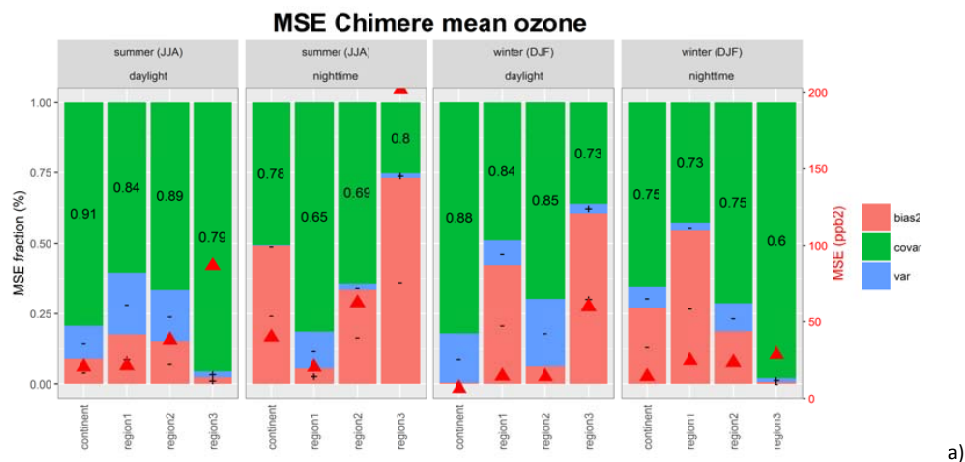
947



966 **FIGURE 6.** CMAQ MSE breakdown for summer and winter for the base case and sensitivity simulations over NA. The error coefficients
 967 F_b, F_v, F_c are reported on the left axis, the total MSE (ppb^2) on the right axis (red triangles). The '+' and '-' signs within the bias and variance
 968 portions of the errors indicate model over- or under-prediction of mean concentration or variance, respectively. The values in the
 969 covariance portion indicate the correlation coefficient between modelled and observed time series. a) hourly time series of ozone (base
 970 case); b) hourly time series of '20% reduction' scenario; c) hourly time series of 'zero boundary conditions' scenario; d) hourly time series
 971 of the 'zeroed anthropogenic emissions' scenario; e) base case rolling average daily maximum 8-hour ozone time series. For the analysis of
 972 hourly time series in panels a) – d), results are provided separately for daytime and nighttime. .

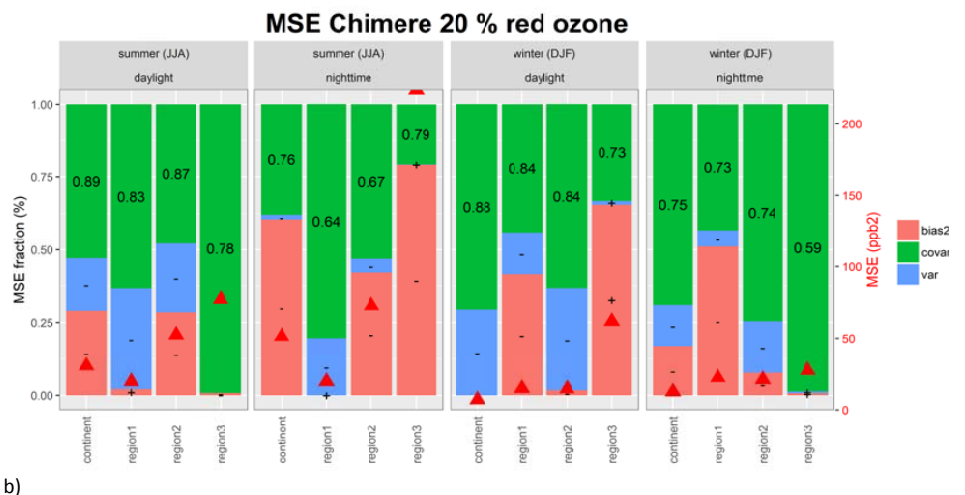


955



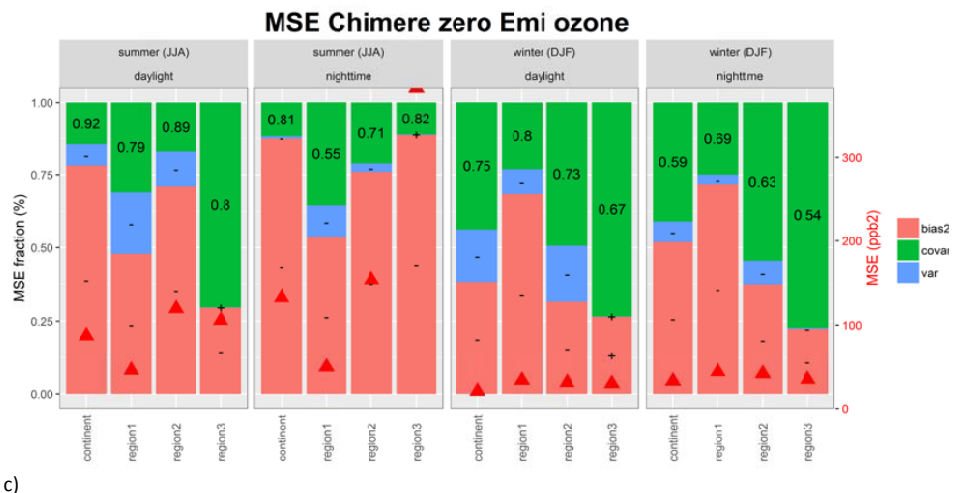
959
960

b)



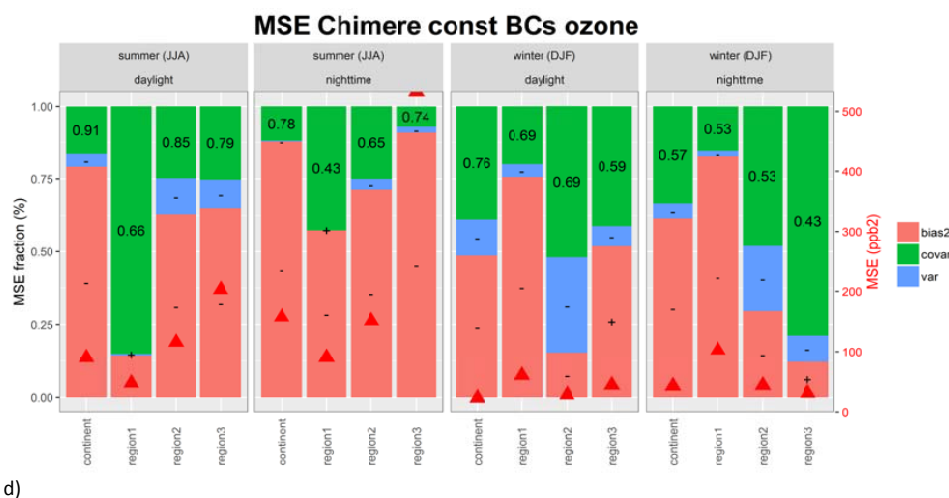
961
962

c)



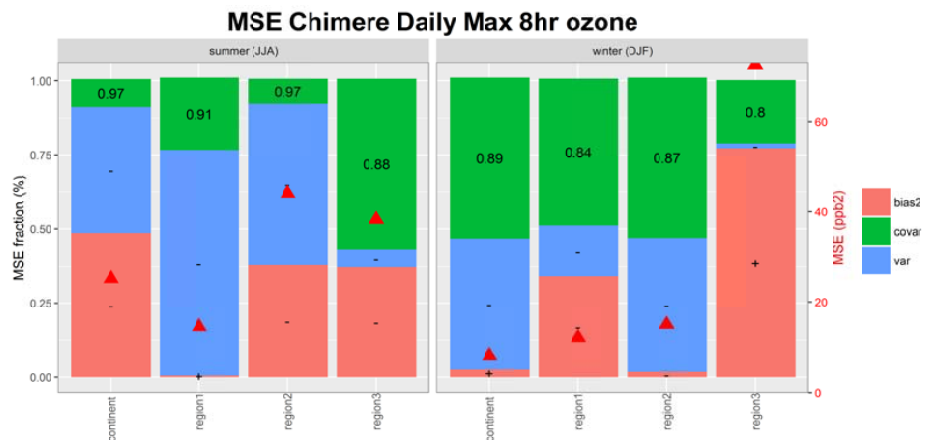


960



964
 965

d)



963

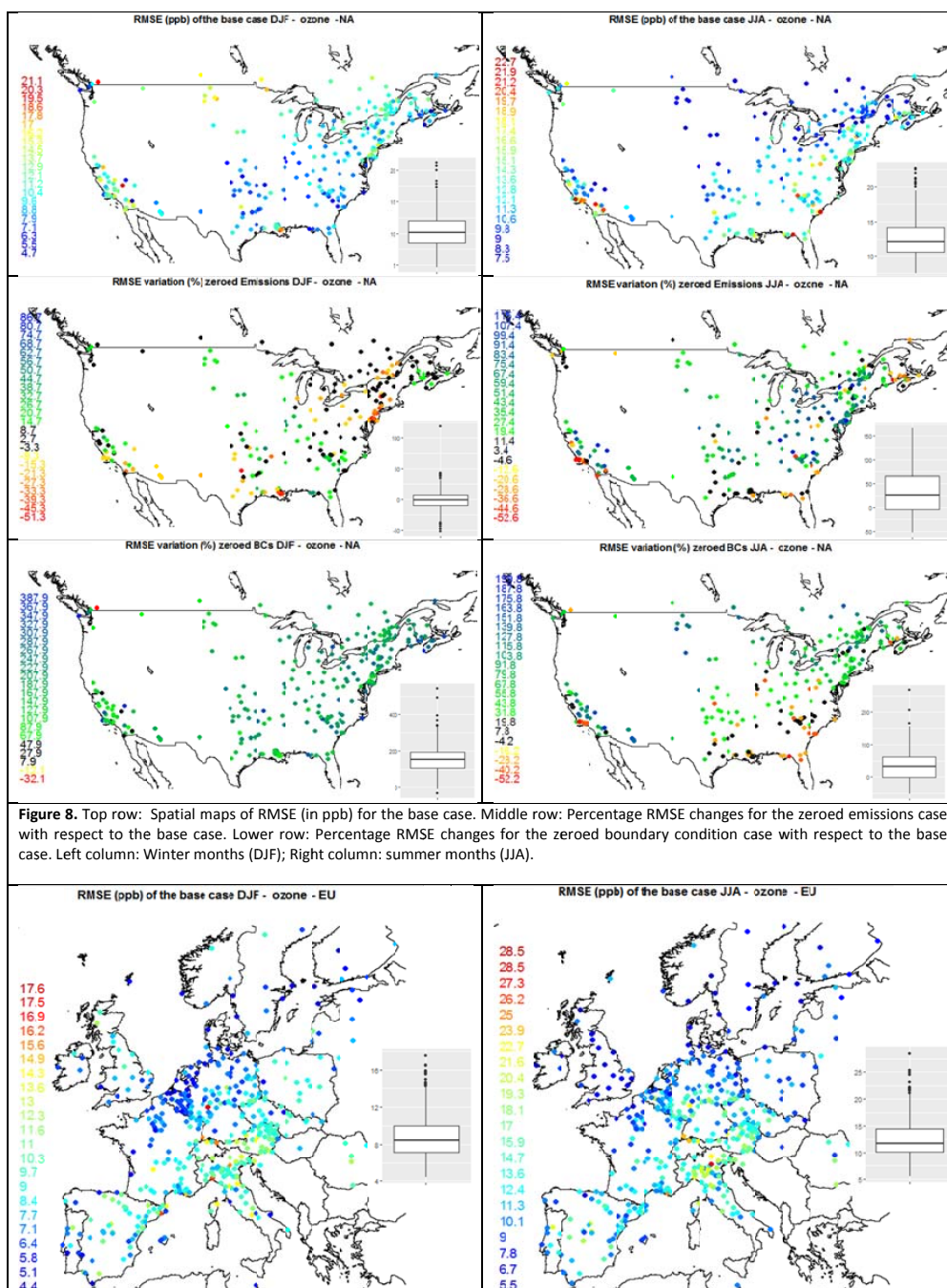
e)

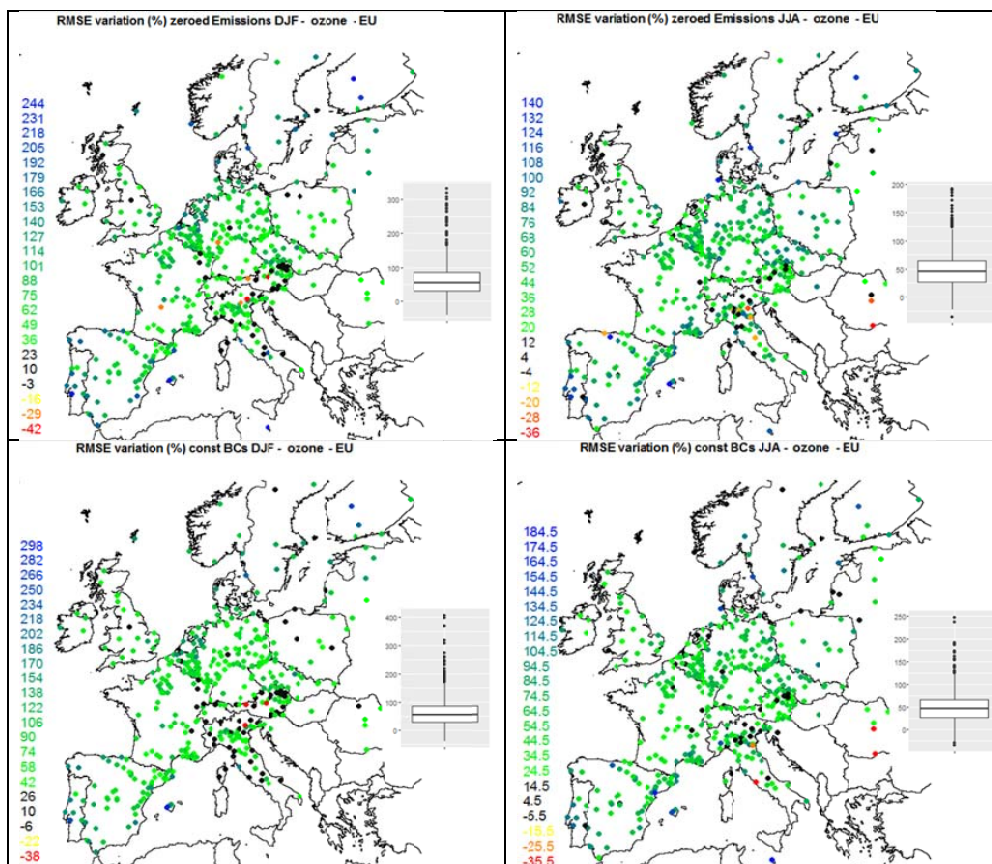
FIGURE 7. Chimere MSE breakdown for summer and winter for the base case and sensitivity simulations over EU. The error coefficients F_b, F_v, F_c are reported on the left axis, the total MSE (ppb^2) on the right axis (red triangles). The '+' and '-' signs within the bias and variance portions of the errors indicate model over- or under-prediction of mean concentration or variance, respectively. The values in the covariance portion indicate the correlation coefficient between modelled and observed time series. *a)* hourly time series of ozone (base case); *b)* hourly time series of '20% reduction' scenario; *c)* hourly time series of 'constant boundary conditions' scenario; *d)* hourly time series of the 'zeroed anthropogenic emissions' scenario; *e)* base case rolling average daily maximum 8-hour ozone time series. For the analysis of hourly time series in panels a) – d), results are provided separately for daytime and nighttime. .

971

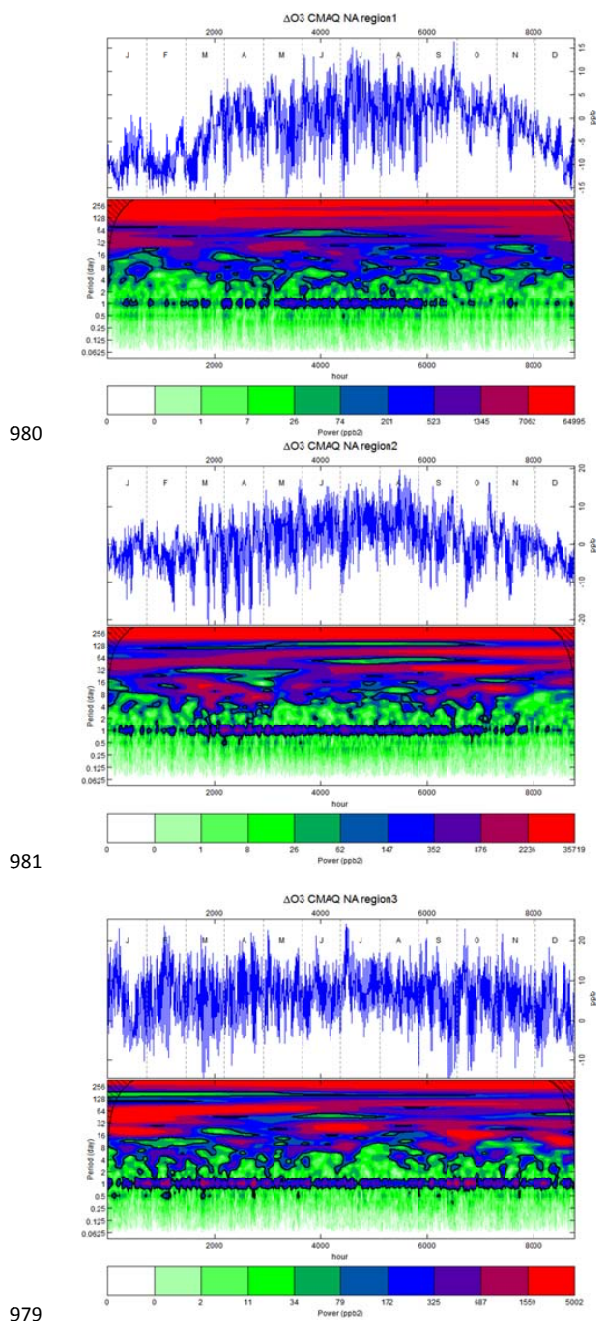
972

973

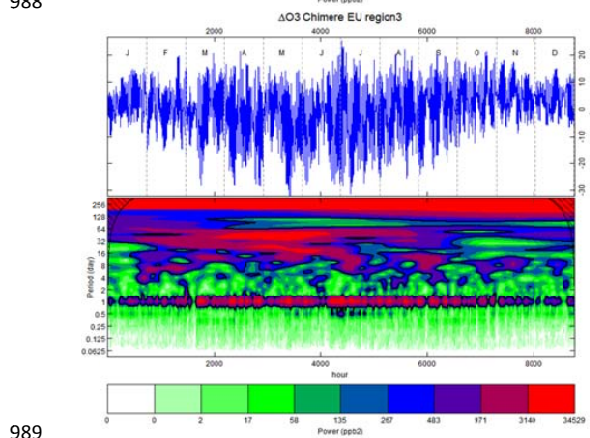
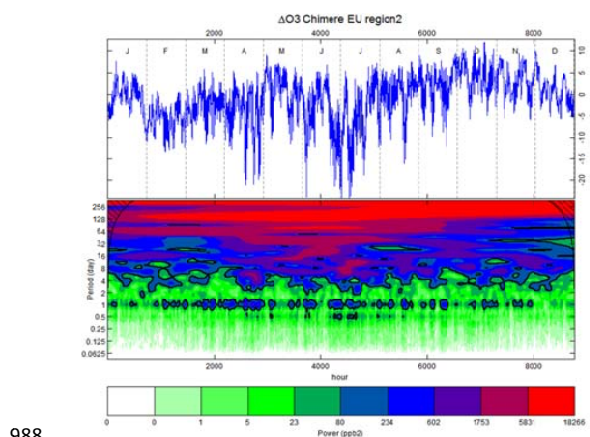
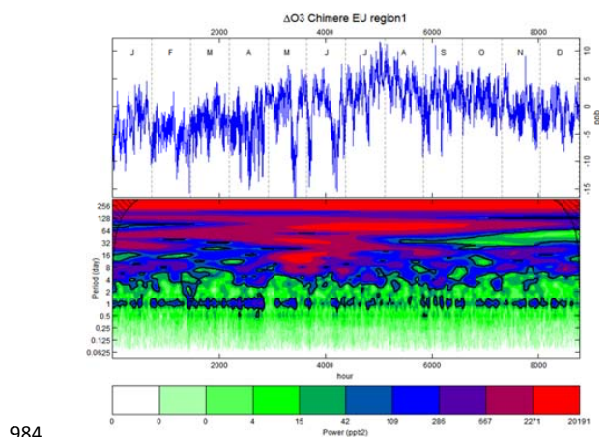




980 **FIGURE 9.** Top row: Spatial maps of RMSE (in ppb) for the base case. Middle row: Percentage RMSE changes for the zeroed emissions case
 981 with respect to the base case. Lower row: Percentage RMSE changes for the constant boundary condition case with respect to the base
 982 case. Left column: Winter months (DJF); Right column: summer months (JJA).

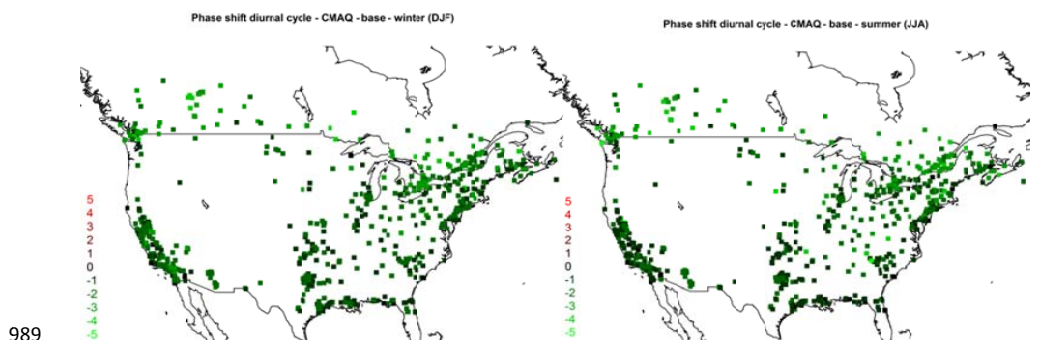


987 **FIGURE 10.** Annual time series of differences between CMAQ and observed O_3 (ΔO_3 , top panel) and Morlet wavelet analysis of the
988 periodogram of ΔO_3 (lower panel) for the three NA subdomains. Black contours lines identify the 95% confidence interval. The period (in
989 days) is reported in the vertical axis, while the quantiles of the power spectral density are measured in ppb^2 .



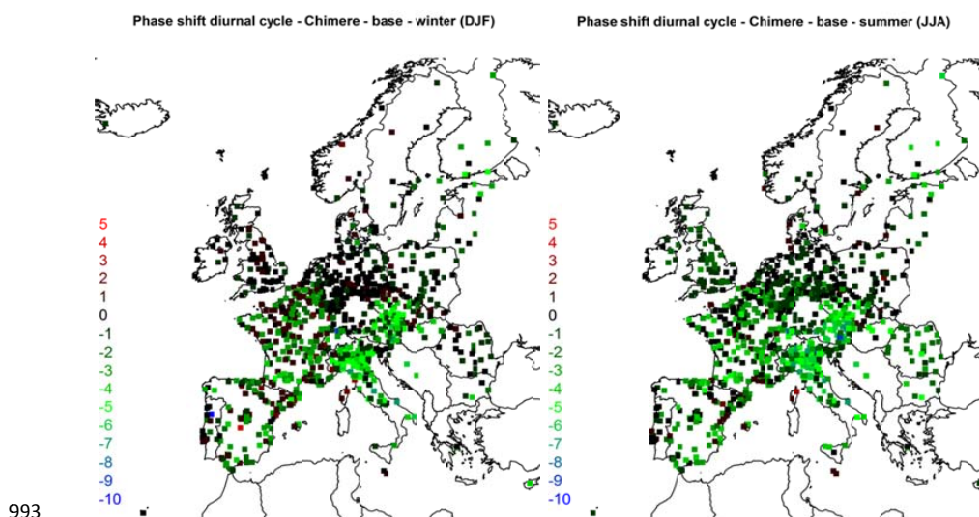
987 **FIGURE 11.** As in Figure 10 for Chimere over the three EU subdomains.

988



989

996 **Figure 12.** Phase shift of the diurnal cycle (in hours). A positive phase shift indicates that the model peak is 'late', while a negative phase
997 shift indicates that the modelled peak precedes the observed peak. This analysis includes urban and suburban stations in addition to rural
998 stations.

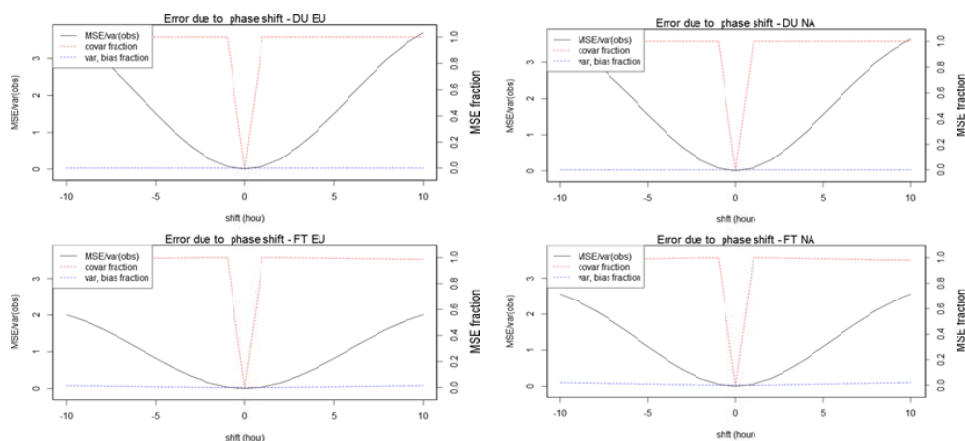


993

994 **FIGURE 13.** As in Figure 12 for EU.

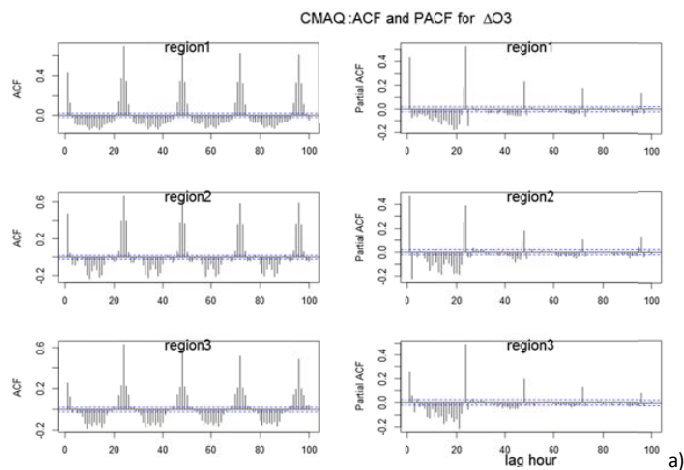
995

996

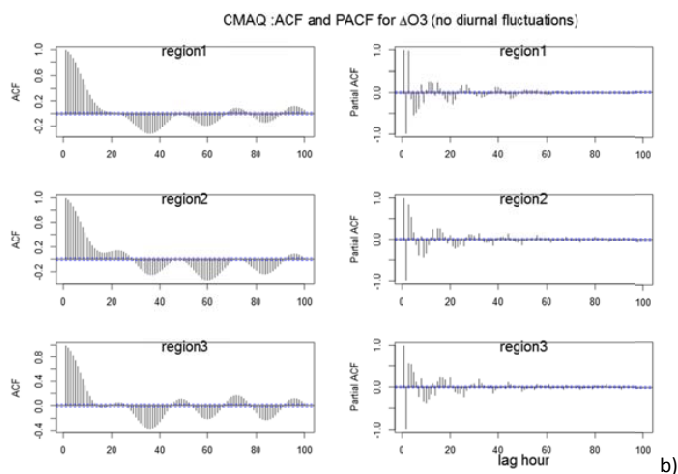


997

1007 **FIGURE 14.** Normalised MSE produced by lagging the observed diurnal cycle with respect to itself. The MSE due to such a shift is entirely
 1008 due to covariance error. The plots are presented for EU2 (left) and NA2 (right) for the months of JJA. The top panel shows the impact of
 1009 the phase shift on the DU component, and the lower panels show results for the undecomposed time series (FT). For EU2, a shift of ± 3
 1010 hours causes an MSE of -0.5 times the variance of the observations.

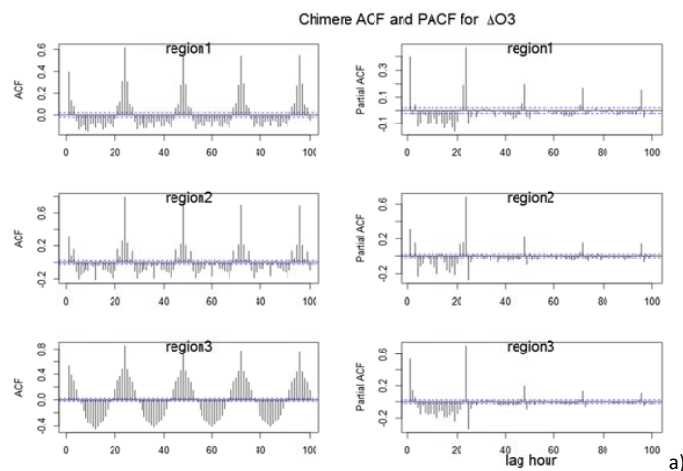


1002

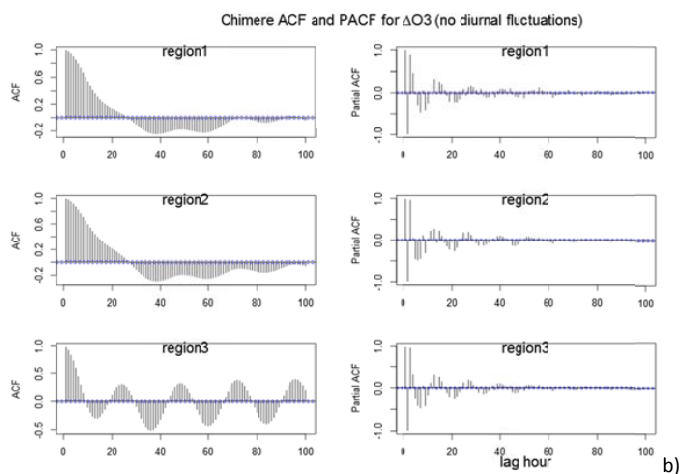


1003

1013 **FIGURE 15.** CMAQ model: autocorrelation (ACF) and partial autocorrelation (PACF) function for *a)* the differenced time series of residuals
1014 of ozone (mod-obs) and *b)* the differenced time series of residual of ozone obtained by filtering out the diurnal fluctuations from the
1015 modelled and observed time series. The differentiation is necessary to remove non-stationarity and thus to make the the acf and pacf
1016 values depending on lag only.



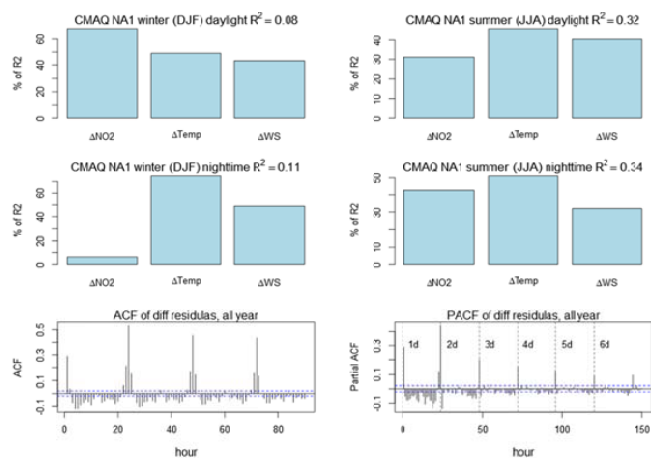
1008



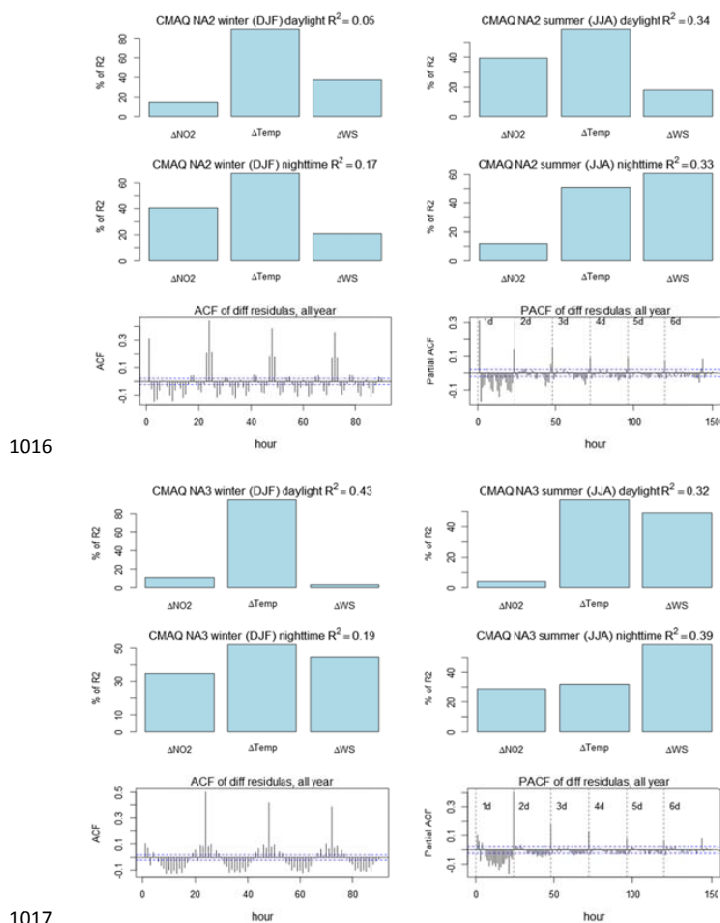
1009

1019 **FIGURE 16.** Chimere model: autocorrelation (ACF) and partial autocorrelation (PACF) function for *a)* the differenced time series of
 1020 residuals of ozone (mod-obs) and *b)* the differenced time series of residual of ozone obtained by filtering out the diurnal fluctuations from
 1021 the modelled and observed time series. The differentiation is necessary to remove non-stationarity and thus to make the ACF and PACF
 1022 values depending on lag only.

1014



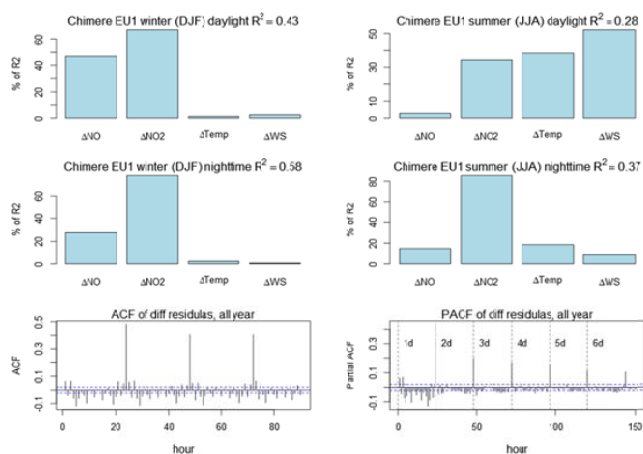
1015



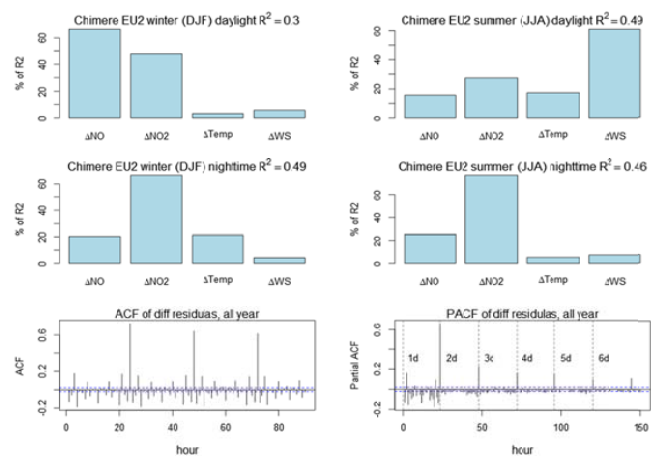
1027 **FIGURE 17.** Percentage of variance explained by the regressors (the total R^2 for the regression is reported in the title of each panel). The
 1028 relative importance of each variable is assessed by using a bootstrap resampling. The plots at the bottom show the ACF and PACF of the
 1029 yearly time series of residual of the fit, i.e. the portion of the ozone time series that was not captured by the linear regressions on the
 1030 available variables.



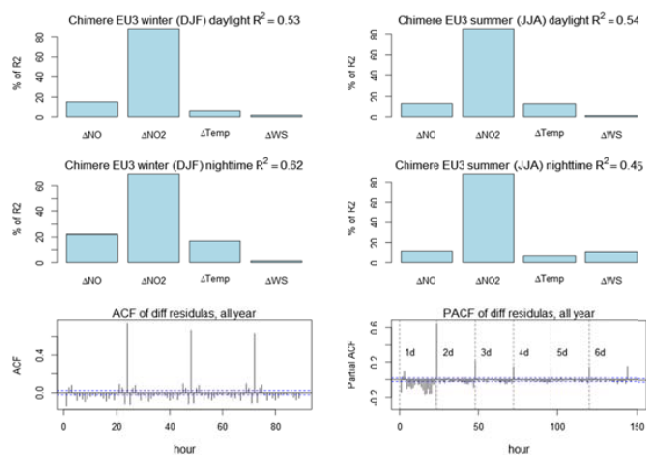
1022



1023



1024



1025 **FIGURE 18.** Same as Figure 17 for EU.

1026